Title: Dysregulated methylation–ubiquitination crosstalk accelerates intervertebral disc degeneration via MED12 destabilization and cGAS/STING activation

Authors: Huaizhen Liang[1†], Dingchao Zhu[1†], Zhi Du[1†], Xinyu Li[1†], Rui Shi[1†], Jie Lei[1], Bide Tong[1], Hanpeng Xu[1], Di Wu[1], Xingyu Zhou[1], Yifan Du[1], Zixuan Ou[1], Junyu Wei[1], Shuchang Peng[1], Wencan Ke[1,2], Zhiwei Liao[1], Bingjin Wang[1], Kun Wang[1], Xiaobo Feng[1], Yu Song[1*], Cao Yang[1*]

Affiliations:

[1] Department of Orthopaedics, Union Hospital, Tongji Medical College, Huazhong University of Science and Technology, Wuhan, 430022, China.

[2] Hubei JiangXia Laboratory, Wuhan, 430071, China.

*Corresponding author.

Cao Yang, Department of Orthopaedics, Union Hospital, Tongji Medical College, Huazhong University of Science and Technology, Wuhan, 430022, China; Shenzhen Huazhong University of Science and Technology Research Institute, Shenzhen 518057, China; e-mail: caoyangunion@hust.edu.cn.

Yu Song, Department of Orthopaedics, Union Hospital, Tongji Medical College, Huazhong University of Science and Technology, Wuhan, 430022, China; e-mail: songyu1277@hust.edu.cn.

† These authors contributed equally to this work： Huaizhen Liang, Dingchao Zhu, Zhi Du and Xinyu Li, Rui Shi.

Abstract

Intervertebral disc degeneration (IVDD) is a leading cause of low back pain, yet clinically, there remains no effective therapeutic approach to reverse its progression, imposing a substantial socioeconomic burden. While multiple factors contribute to IVDD pathogenesis, cellular senescence has emerged as a critical risk factor associated with both the incidence and progression of IVDD. Ageing and other damage factors drive nucleus pulposus cells (NPCs) towards a senescent phenotype characterized by increased secretion of proinflammatory factors, resulting in NPC dysfunction and tissue degeneration, which are hallmarks of IVDD. In this study, we demonstrated that PRMT2 deficiency disrupted arginine methylation–ubiquitination crosstalk, driving NPC inflammatory senescence and accelerating IVDD progression. Mechanistically, PRMT2 loss reduced FBXO7 methylation at Arg 504, promoting the FBXO7-MED12 interaction to facilitate MED12 ubiquitination and subsequent proteasomal degradation. MED12 deficiency induced pathological R-loop accumulation, which activated the cytosolic DNA-sensing cGAS-STING axis, triggering inflammatory response cascades. Notably, engineered extracellular vesicles (EVs) delivering MED12-overexpressing plasmids significantly inhibited NP cell senescence and attenuated IVDD progression. Together, our findings establish that dysregulated methylation–ubiquitination crosstalk critically drives IVDD progression and reveal MED12 as a promising therapeutic target for ameliorating the impact of IVDD.

Graphical abstract

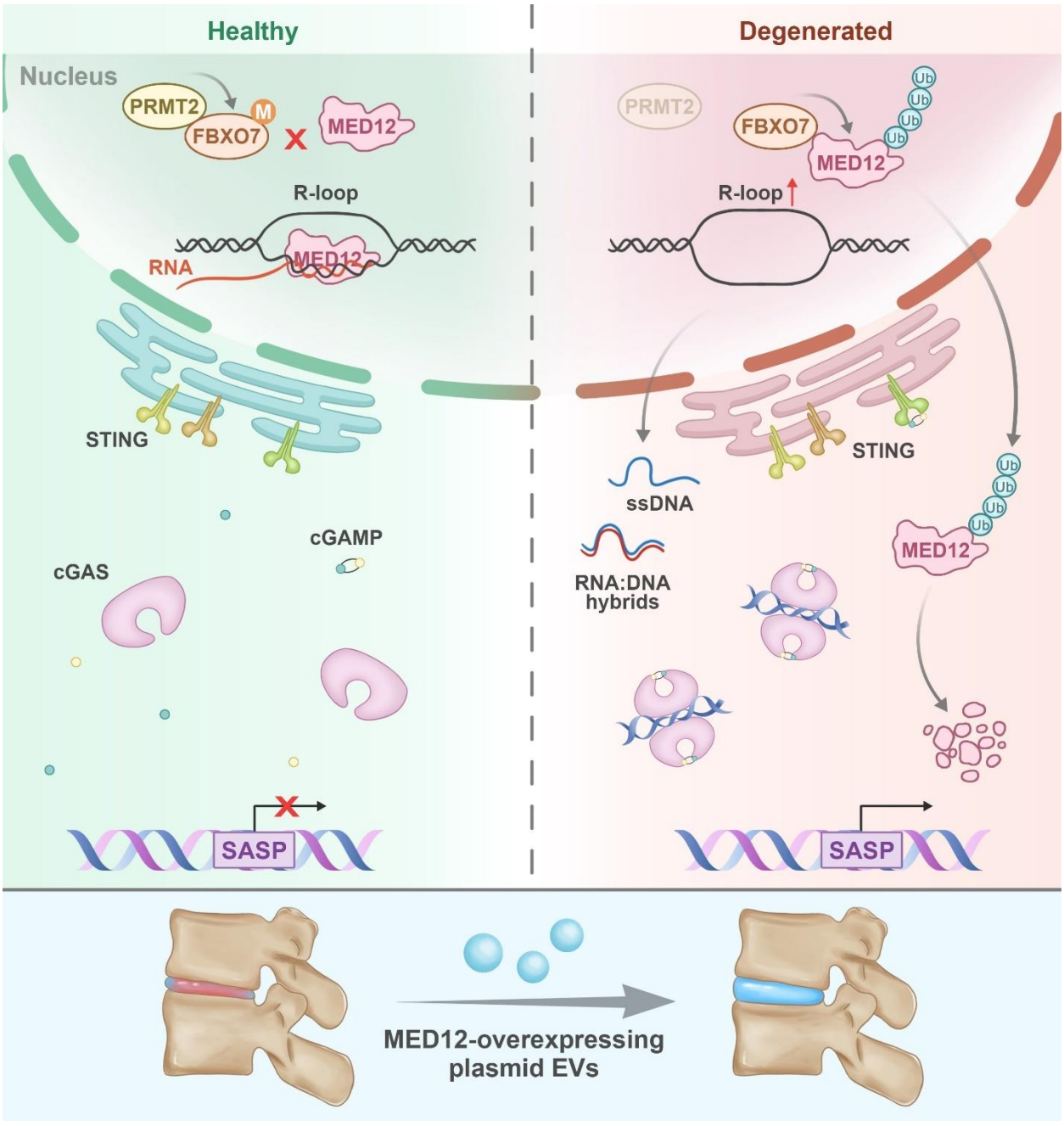

Introduction

Intervertebral disc degeneration (IVDD) is a geriatric disease that is becoming increasingly prevalent in modern society(1). It manifests itself primarily as low back pain (LBP), which severely affects a patient's daily life and ability to work(2, 3). The incidence of IVDD continues to rise as the global population ages and sedentary lifestyles become more common. Ageing and various injury factors contribute to the conversion of NPCs to a proinflammatory and hypersecretory senescent phenotype, leading to dysfunction of NPCs and tissue inflammation and degeneration, which can cause the development of IVDD(4-7). An in-depth analysis of the regulatory mechanisms of NP senescence is highly important for exploring clinical therapeutic strategies for IVDD.

Posttranslational modifications (PTMs) play pivotal roles in the intricate cellular signalling pathways(8, 9). PTMs do not act in isolation, and the interplay between different types of PTMs is emerging as an important dimension of cellular regulation that fine-tunes cellular responses to environmental cues(10, 11). Among the various PTMs, arginine methylation has received much attention because of its prevalence and importance in cellular processes(9, 12). Arginine methylation involves the addition of a methyl group to the nitrogen atom of an arginine residue, a modification that affects protein–protein interactions, protein stability, and enzyme activity(13-15). However, the interplay between arginine methylation and other PTMs remains poorly understood. Interestingly, our mass spectral analysis revealed significant changes in the arginine methylation levels of FBXO7 during IVDD progression. FBXO7 is a member of the F-box protein (FBP) family and constitutes the substrate-recruiting subunit of the Skp1-Cullin1-F-box protein (SCF) ubiquitin E3 ligase complex(16, 17). The arginine methylation of the ubiquitin substrate aptamer FBXO7 observed in our study prompted us to explore whether this PTM

interplay is involved in IVDD progression and to identify the underlying molecular mechanisms involved.

Surprisingly, our proteomic analysis revealed MED12 as the most prominent target of methylation–ubiquitination crosstalk, which involves ubiquitin-dependent protein degradation during IVDD development. MED12, a member of the Mediator complex, is a multifunctional protein that acts as a platform to interact with histone-modifying enzymes, coactivators, transcription factors, and the Mediator complex to regulate epigenetic landscapes and gene expression(18-21). Given that MED12 is a universally required coordinator of nuclear homeostasis regulation, its role in cellular senescence and the development of age-related IVDD warrants further exploration.

In this study, we report that during IVDD progression, the PRMT2 deficiency–mediated loss of arginine methylation of FBXO7 leads to aberrant R-loop formation and promotes inflammatory senescence in NP cells. Mechanistically, loss of PRMT2 leads to reduced arginine methylation of FBXO7, which promotes ubiquitin-dependent protein degradation of MED12 by increasing the interaction of FBXO7 with MED12. Thus, MED12 deficiency causes R-loop accumulation, triggering an inflammatory cascade response through the activation of DNA sensing-related signalling pathways. Notably, extracellular vesicles (EVs) loaded with MED12-overexpressing plasmids significantly alleviated NPC senescence and the progression of IVDD.

Results

FBXO7 methylation deficiency promotes NPC senescence and IVDD progression

To comprehensively analyse the dynamics of methylated proteins during IVDD, we employed a label-free quantitative proteomics approach using a pan-methylated antibody to enrich methylated peptides from total protein extracts of healthy and degenerated NP tissues (Figure 1A). We quantified 158 mono-methylarginine (MMA) sites in more than half of the biological replicates, with 125 methylated sites quantified in degenerated samples and 131 methylated sites quantified in healthy samples. Strikingly, we observed MMA at position 504 of FBXO7 in all the biological replicates of the healthy samples, yet it was consistently absent in the degenerated samples (Figure 1, B and C, and Supplemental Figure 1A). Next, we verified the presence of arginine methylation in FBXO7. We exogenously expressed the FBXO7 protein fused with a GFP tag in HEK293T cells, which were immunoprecipitated and then subjected to western blotting using a pan-anti-mono-methylarginine antibody, which revealed MMA of FBXO7. Moreover, its methylation level decreased in a dose-dependent manner following treatment with the protein arginine methyltransferase (PRMT) inhibitor adenosine dialdehyde (AdOx) (Figure 1D)(22). Furthermore, we used TBHP to establish an in vitro senescence model of NPCs, and our results showed that treatment with 50 μM TBHP for 5 days induced a stable senescent phenotype (Supplemental Figure 2, A–D). We observed that arginine methylation of endogenous FBXO7 was significantly decreased in TBHP-induced degenerated NPCs (Figure 1E). Next, we introduced arginine-to-lysine (RK) and arginine-to-phenylalanine (RF) substitutions at position 504 of FBXO7. RK substitution achieved methylation deficiency in FBXO7, whereas the RF substitution mimics a constitutive methylation in FBXO7(23, 24). As expected, the RK FBXO7 mutant presented a marked reduction in methylation levels relative to those of wild-type (WT)

FBXO7. Furthermore, TBHP treatment elicited significant inhibition of methylation in WT FBXO7, whereas the RK mutant showed no further reduction in methylation compared with the basal state (Supplemental Figure 1B). To specifically detect arginine methylation at position 504 of FBXO7, we generated a site-specific methylation antibody. Dot blot analysis confirmed its specificity (Supplemental Figure 1, C and D). In both TBHP-induced and replication stress-induced senescence models of NPCs, we consistently observed a marked downregulation of FBXO7-R504me levels (Figure 1, F and G). Furthermore, we validated the decreased levels of FBXO7-R504me in another independent cohort of human nucleus pulposus (NP) tissues with intervertebral disc degeneration (Figure 1H and Supplemental Figure 1E). Immunofluorescence staining revealed that FBXO7-R504me was downregulated in the NP tissue concomitant with disc degeneration, whereas its levels remained unchanged in the endplate (Figure 1I). Collectively, these data demonstrated that FBXO7 undergoes methylation at Arg504.

The observed absence of Arg504 methylation in FBXO7 cells from degenerated NPCs prompted us to investigate its potential causal role in IVDD pathogenesis. We transduced wild-type FBXO7 or RF substitution FBXO7 mutant plasmids into FBXO7-deficient NPCs through recombinant expression. TBHP treatment induced a marked cellular senescence phenotype in NPCs transduced with WT FBXO7, as evidenced by significant upregulation of senescence-associated markers, accumulation of phosphorylated γH2AX foci, and markedly reduced EdU incorporation rates(25). In contrast, the recombinant RF mutant conferred resistance to the TBHP-triggered senescence phenotype (Supplemental Figure 2, E–H). To systematically investigate the in vivo functional consequences of FBXO7 Arg504 methylation in IVDD, we established a validated caudal IVDD rat model through needle puncture. In this model, endogenous FBXO7 was first knocked down via intradiscal delivery of adeno-associated virus

(AAVs) expressing FBXO7 short hairpin RNA (shRNA), followed by reconstitution with either wild-type FBXO7 or the RF substitution mutant (Supplemental Figure 2, I–L). MRI evaluation demonstrated that T2-weighted MRI signal intensity significantly decreased with needle puncture in IVDs transduced with WT FBXO7 plasmids, whereas the magnitude of signal loss was significantly attenuated in IVDs transduced with RF mutant plasmids (Figure 2D and Supplemental Figure 2M)(26). Integrated X-ray and micro-CT analyses revealed that reconstitution with the FBXO7 RF mutant significantly attenuated disc height loss in needle puncture-induced degenerative discs compared with IVDs reconstituted with WT FBXO7 (Figure 2E and Supplemental Figure 2M). Moreover, histological staining indicated that the reconstitution of RF mutants in IVDs attenuated the needle puncture-induced degenerated phenotype, as indicated by improved extracellular matrix organization, distinct anatomical demarcation between the NP and annulus fibrosus (AF) regions, and relative preservation of the NP volume compared with those of WT FBXO7-reconstituted discs (Figure 2, A and C)(27). Importantly, immunohistochemical (IHC) and immunofluorescence staining demonstrated that, compared with WT FBXO7-reconstituted discs, intervertebral discs reconstituted with the RF mutant presented significantly lower proportions of phosphorylated p53-positive (p-p53$^+$) , γH2A-positive (γH2A$^+$), p21-positive (p21$^+$) and IL-1β (IL-1β$^+$) NPCs (Figure 2B). Collectively, these findings demonstrated that pathological loss of FBXO7 Arg504 methylation might drive IVDD progression.

Loss of PRMT2-mediated FBXO7 Arg504 methylation promoted NP cell senescence and IVDD progression

To identify methyltransferases capable of methylating FBXO7, we conducted a comprehensive PRMT family screen by coexpressing GFP-FBXO7 with HA-tagged PRMTs (PRMT1-8) in HEK293T cells. Coimmunoprecipitation (co-IP) analysis showed that only PRMT2 interacted with FBXO7 but not with other PRMTs (Figure 3A). The PRMT2-FBXO7 interaction was validated through reciprocal co-IP in HEK293T cells (Figure 3B and Supplemental Figure 3A). Consistently, the binding of endogenous PRMT2 and FBXO7 was detected in NPCs (Figure 3C). FBXO7 contains several domains: a ubiquitin-like (UBL) domain, a FBXO7-PI31 dimerization (FP) domain, an F-box domain, and a proline-rich motifs (PRMs)(17). We demonstrated that deletion of the C-terminal PRR abrogated the interaction between FBXO7 and PRMT2 (Supplemental Figure 3, B and C)(28). The N-terminal SH3 domain of PRMT2 is known to mediate specific recognition of PRMs in binding partners(29, 30). Our findings revealed that the SH3 domain is necessary for the interaction of PRMT2 with FBXO7 (Figure 3D and Supplemental Figure 3B). Together, these findings demonstrate that PRMT2 directly interacts with FBXO7. Furthermore, we explored whether FBXO7 is methylated by PRMT2. Reconstitution of full-length (FL) PRMT2 or SH3 domain-deleted PRMT2 (ΔSH3-PRMT2) in endogenous PRMT2-depleted HEK293T cells revealed that PRMT2 depletion or expression of ΔSH3-PRMT2 significantly reduced FBXO7 methylation in contrast to that in control cells or cells reconstituted with FL PRMT2 (Figure 3E and Supplemental Figure 3D). Moreover, overexpression of PRMT2 significantly increased the methylation level of WT-FBXO7 but not the RK mutant (Figure 3F). These findings indicate that PRMT2 is essential and capable of catalysing FBXO7 methylation at Arg504.

We next investigated how PRMT2 is regulated in the context of IVDD. Immunohistochemistry and quantitative real-time PCR revealed that PRMT2 levels were downregulated in degenerated

intervertebral discs (Figure 3, G and H). To explore the mechanism underlying PRMT2 downregulation, we used the JASPAR database to predict transcription factors that may bind to the PRMT2 promoter. HIF1α was predicted to bind at a site located −139 to −134 upstream of the PRMT2 transcription start site (Figure 3I). HIF1α, a master transcriptional regulator of cellular adaptation to hypoxia, plays a critical protective role in IVDD by maintaining mitochondrial integrity, promoting glycolysis, reducing oxidative stress and apoptosis, and its expression is progressively downregulated in degenerated NP tissues, correlating with disease severity. Chromatin immunoprecipitation–polymerase chain reaction (ChIP-PCR) analysis demonstrated that both TBHP treatment and HIF1α knockdown reduced HIF1α enrichment at the PRMT2 promoter (Figure 3, J and K). Consistently, knockdown of HIF1α downregulated PRMT2 expression under both normoxic and hypoxic conditions (Supplemental Figure 3, E and F). To validate the functional role of HIF1α in regulating PRMT2 expression and disc degeneration in vivo, we injected AAVs expressing Hif1α shRNA into rat caudal intervertebral discs. H&E and immunohistochemical staining revealed that the sh-HIF1α group exhibited more severe disc degeneration and concomitantly lower PRMT2 levels compared to the control group (Figure 3L). Together, these findings demonstrate that HIF1α transcriptionally regulates PRMT2 expression, and the loss of HIF1α during IVDD contributes to PRMT2 downregulation and accelerated disc degeneration.

Next, we explored the functional consequences of PRMT2-mediated FBXO7 Arg504 methylation on NP cell senescence. PRMT2 knockdown triggered a senescence-associated phenotype characterized by elevated expression of classical senescence markers, persistent accumulation of DNA damage foci, and profound inhibition of proliferative capacity. Importantly, reconstitution of wild-type PRMT2, but not its SH3 domain-deficient variant,

effectively attenuated these senescence-associated phenotype changes (Supplemental Figure 3, G–I). Furthermore, intradiscal delivery of PRMT2-targeting shRNA via an adeno-associated virus into the rat caudal spine induced distinct degenerative phenotypes. Radiographic assessment demonstrated significant disc height reduction, paralleled by diminished MRI T2-weighted signal intensity indicative of NP dehydration (Figure 3, M, Q and R). Histopathological evaluation revealed structural hallmarks of degeneration, including a contracted NP area with extracellular matrix disorganization and disrupted annulus fibrosus lamellar architecture (Figure 3, N and P). Strikingly, PRMT2 knockdown in vivo significantly increased the expression of p-p53, γH2AX, p21, and IL-1β (Figure 3O). Conversely, compared to the AAV-Control group, intradiscal delivery of AAV-PRMT2 for PRMT2 overexpression markedly attenuated puncture-induced disc degeneration, as evidenced by preserved disc height, T2 signal intensity, NP matrix integrity, and organized annulus fibrosus architecture, along with reduced expression of p-p53, γH2AX, p21, and IL-1β (Supplemental Figure 4, A–F). Taken together, these results establish that deficiency in the PRMT2-mediated methylation of FBXO7 at Arg504 promotes both NP cell senescence and IVDD progression.

FBXO7 Arg504 methylation prevents FBXO7-mediated MED12 recruitment and destabilization

Building upon the established role of FBXO7 Arg504 methylation in mitigating IVDD, we propose elucidating the molecular cascade through which this modification regulates disease pathogenesis. FBXO7 functions as the substrate-recruiting subunit of the SCF E3 ubiquitin ligase complex, with its substrate recognition dynamics potentially modulated by PTMs(31, 32). Exogenous co-IP and mass spectrometry were performed to identify the FBXO7-binding protein

from wild-type FBXO7 or RK mutant transduced HEK293T cells. We identified 201 potential FBXO7-binding partners in RK mutant-expressing HEK293T cells and 97 candidates that interact with wild-type FBXO7 (Figure 4A). Further proteomic profiling of endogenous FBXO7 interactomes through anti-FBXO7 co-IP coupled with mass spectrometry revealed substantial remodeling of binding partners between normal and degenerated NPCs. Notably, 7 proteins within the FBXO7 RK mutant interactome exhibited enhanced interactions with FBXO7 in degenerated NP cells. Among them, MED12 was identified as the most significantly enriched protein among the FBXO7-binding proteins in degenerated NPCs (Figure 4A). Consistently, co-IP assays confirmed that MED12 exhibited the strongest interaction with FBXO7 among these seven candidate proteins (Supplemental Figure 5A). As a critical component of the Mediator complex, MED12 plays a role in transcriptional initiation and epigenetic regulation, either in a Mediator-dependent or Mediator-independent manner(33, 34). Based on these findings, we proceeded to inquire into the mode of interaction between FBXO7 and MED12. Reciprocal coimmunoprecipitation (co-IP) assays demonstrated a direct interaction between endogenous FBXO7 and MED12 in NPCs (Figure 4B). To further validate this interaction, exogenous coexpression experiments in HEK293T cells revealed specific coprecipitation of GFP-tagged FBXO7 with FLAG-tagged MED12 and vice versa (Figure 4C and Supplemental Figure 5B). To map the interaction domains between FBXO7 and MED12, we performed co-IP assays in HEK293T cells expressing truncated variants of both proteins. Domain mapping analysis revealed that the C-terminal region of MED12 and the UBL domain coupled with the FP domain of FBXO7 are essential for their physical interaction (Supplemental Figure 5, C–E)(35). To investigate how FBXO7 Arg504 methylation regulates its interaction with MED12, we performed co-IP assays in HEK293T cells expressing WT FBXO7 or a constitutively methylated

RF mutant. Treatment with the methylation inhibitor AdOx markedly enhanced the interaction between WT FBXO7 and MED12, whereas the RF mutant was less sensitive to AdOx (Figure 4D). Furthermore, we performed co-IP assays in HEK293T cells expressing wild-type FBXO7, methylation-resistant RK mutants, or constitutively methylated RF mutants. Strikingly, the RF mutant markedly reduced the FBXO7-MED12 interaction, whereas the WT and RK mutants retained MED12 binding capacity (Figure 4E). Moreover, western blot analysis demonstrated reduced MED12 protein levels in degenerated NP tissues, showing an inverse correlation with the senescence phenotype of disc degeneration (Supplemental Figure 5, F and G). To determine whether FBXO7-mediated recruitment of MED12 facilitates its proteolytic turnover, we assessed MED12 protein levels in NPCs overexpressing WT FBXO7 or RK/RF mutants. WT and RK mutants markedly decreased MED12 levels in a dose-dependent manner, whereas the RF mutant failed to reduce MED12 levels (Figure 4G). Furthermore, pharmacological inhibition of methylation using AdOx reduced MED12 protein levels and destabilized MED12 in HEK293T cells expressing wild-type FBXO7 but not the RF mutant (Figure 4F and Supplemental Figure 5H). Collectively, these findings demonstrated that pathological loss of FBXO7 Arg504 methylation increased the FBXO7-MED12 interaction, thereby leading to increased MED12 destabilization.

FBXO7 Arg504 methylation impedes FBXO7-mediated K48-linked ubiquitination of MED12

Given the demonstrated physical interaction between FBXO7 and MED12 and their functional linkage in promoting MED12 destabilization, we propose a mechanistic model in which FBXO7 directly catalyses MED12 polyubiquitination, thereby leading to its proteasomal degradation

(Figure 5A). The decrease in MED12 protein levels induced by FBXO7 overexpression was blocked by the proteasome inhibitor MG132 but not by the lysosomal inhibitor BafA1 (Figure 5, B and C). Consistently, the half-life of the endogenous MED12 protein were significantly reduced under FBXO7 overexpression, as demonstrated by protein stability assays using cycloheximide (CHX) treatment (Figure 5D). Furthermore, co-IP experiments demonstrated significantly elevated ubiquitination levels of MED12 in degenerated NPCs from pairs of human samples (Figure 5E). We observed that MED12 ubiquitination was decreased upon FBXO7 knockdown (Figure 5F). However, overexpression of wild-type FBXO7, but not the catalytically inactive F-box domain-deleted ΔF-FBXO7 mutant, strongly increased MED12 ubiquitination (Figure 5G)(17). Given that K48-linked ubiquitin chains are canonical signals for proteasomal recognition and degradation, we next sought to characterize the type of FBXO7-catalysed ubiquitin chains on MED12(36). In HEK293T cells reconstituted with the ubiquitin-K48R mutant (defective in the formation of K48-linked ubiquitin chains), FBXO7 overexpression failed to increase MED12 ubiquitination levels, whereas this impairment was not observed with the ubiquitin-K63R mutant (Figure 5H). Furthermore, FBXO7 overexpression markedly promoted K48-linked polyubiquitin chain formation in MED12 (Figure 5I). Collectively, these findings establish that FBXO7 selectively targets MED12 for proteasomal degradation through K48-linked ubiquitination.

We subsequently investigated the impact of FBXO7 methylation on MED12 K48-linked ubiquitination. Co-IP assays demonstrated that AdOx treatment markedly elevated MED12 ubiquitination levels, whereas HEK293T cells expressing the constitutively methylation-mimetic RF mutant exhibited resistance to AdOx-induced ubiquitination (Figure 5J). Furthermore, transfection of HEK293T cells with WT FBXO7 or RF or RK mutants revealed that the

methylation-mimetic RF mutant significantly reduced MED12 ubiquitination levels compared with those of both the WT and RK variants (Figure 5K). Collectively, these findings demonstrate that FBXO7 Arg504 methylation suppresses the K48-linked ubiquitination of MED12, thereby attenuating its proteasomal degradation. To predict potential ubiquitination sites on MED12, GPS-Uber—a hybrid learning framework integrating deep neural networks and logistic regression for E3-specific ubiquitination site prediction—was employed(37). With a confidence cut-off score of 0.6, the following lysine residues were identified as candidate ubiquitination sites: K429, K762, K785, K1001, K219, K1634, K1643, K1664, K1673, and K1674 (Supplemental Figure 6A). To validate the predicted ubiquitination sites in MED12, WT MED12 plasmids and lysine-to-arginine ubiquitination-defective mutants were transfected into HEK293T cells. Co-IP followed by western blotting revealed that only the K1674R mutation significantly attenuated the K48-linked ubiquitination of MED12, demonstrating that K1674 is a critical ubiquitination site in MED12 (Figure 5L). Consistently, compared with wild-type MED12, FBXO7 overexpression did not increase the ubiquitination level of the K1674 mutant (Figure 5M). Taken together, these findings demonstrate that Arg504 methylation of FBXO7 suppresses MED12 K1674 ubiquitination and proteasomal degradation.

MED12 deficiency promoted cGAS-STING axis-dependent NPC senescence during IVDD progression

On the basis of the observed characteristic loss of MED12 during IVDD, we next sought to systematically investigate its functional role in intervertebral disc pathophysiology. RNA sequencing was performed on NP cells treated with si-Scramble or si-MED12-1 (Supplemental Figure 7A). Gene set enrichment analysis (GSEA) analysis revealed that genes upregulated in the

siMED12-1 group were significantly enriched in DNA damage-related pathways and inflammatory response pathways, including “Senescence associated secretory penotype”, “TNFA signalling via NFKB”, “P53 pathway” and “Inflammatory response”. In contrast, genes upregulated in the si-Scramble group were enriched in extracellular matrix-related pathways, including “ECM Proteoglycans”, “ECM Organization” and “G2M Checkpoint”. (Figure 6, A and B). Volcano plot analysis showed widespread upregulation of NF-κB-related genes in MED12-knockdown NPCs (Figure 6C). In line with transcriptional dysregulation, genetic depletion of MED12 in normal NPCs a senescence-associated inflammatory phenotype, as evidenced by the upregulation of classical senescence markers, concomitant increase in SA-β-gal activity, pronounced γH2AX foci formation indicative of DNA damage, and increased secretion of proinflammatory cytokines (Figure 6, D–F, Supplemental Figure 7B). Collectively, these results establish that MED12 deficiency induces a proinflammatory NP cell phenotype.

The upstream signalling mechanisms of SASP activation are multifactorial and context dependent and vary across senescence-inducing stimuli(38-42). In MED12-knockdown NP cells, GSEA of RNA-seq data showed aberrant activation of cytosolic DNA-sensing pathways (Figure 6G). Consistent with the transcriptomic findings, western blot analysis revealed that MED12 knockdown in NP cells activated the cGAS-STING pathway, as evidenced by increased p-TBK1 and p-IRF3 levels and a characteristic STING gel mobility shift, compared with scramble control cells (Figure 6H). Strikingly, STING knockdown abrogated the senescence-associated phenotypes induced by MED12 depletion (Supplemental Figure 7C). Furthermore, MED12 depletion mediated by short hairpin RNA targeting MED12 delivered via AAVs to rat tail intervertebral discs induced progressive disc degeneration, which is characterized by structural and cellular pathologies (Figure 6I and Supplemental Figure 7D). MRI T2-weighted imaging

revealed reduced signal intensity in the NP region, concomitant with disc height loss observed via X-ray analysis, collectively reflecting structural compromise (Figure 6, M and N, Supplemental Figure 7E). Histological assessment revealed disrupted extracellular matrix organization in MED12-deficient discs, in contrast with the well-preserved matrix architecture in controls (Figure 6, J and L). Importantly, our results showed that in sh-MED12 rat tailbone IVD, MED12 expression was reduced, accompanied by enhanced expression of senescence-associated markers (Figure 6K). These findings demonstrate that MED12 depletion promoted NP cell senescence in intervertebral discs through a cGAS-STING axis-dependent mechanism.

MED12 loss induces R-loop accumulation, which drives NP cell senescence

To investigate the upstream mechanisms driving SASP activation in MED12-depleted NP cells, we performed immunoprecipitation–mass spectrometry to profile the MED12 interactome. The analysis identified 1,035 candidate MED12-associated proteins, with enrichment analysis revealing significant clustering in RNA processing and DNA metabolic pathways (Figure 7A). Notably, 537 of these interactors overlapped with known R-loop regulators (Figure 7B)(43). Intriguingly, pathological R-loop accumulation triggers cytoplasmic leakage of self-derived single-stranded DNA (ssDNA) and RNA:DNA hybrids, which function as endogenous DAMPs. These aberrant nucleic acids activate cytosolic PRRs, including cGAS, triggering STING-dependent inflammatory cascades(41, 44-46). Thus, we hypothesize that cGAS/STING axis-driven inflammatory cascade activation following MED12 depletion could be attributed to pathological R-loop accumulation. Dot blot and immunofluorescence analyses revealed that MED12 knockdown in NP cells triggered significant R-loop accumulation, as evidenced by increased S9.6 antibody signals. Importantly, administration of RNase H, an enzyme that

specifically targets the RNA:DNA hybrid, resulted in a significant reduction in R-loop levels, precluding nonspecific S9.6 cross-reactivity and clearly attributing the observed signals to RNA:DNA hybrid structures (Figure 7, C and E)(47). We next assessed whether R-loop accumulation was accompanied by cytoplasmic ssDNA accumulation. Consistently, elevated cytoplasmic pathological R-loop accumulation and ssDNA levels were observed in MED12-depleted NP cells (Figure 7D).

To mechanistically dissect the interplay between R-loops, cytosolic ssDNA accumulation, and the MED12-associated inflammatory signature, we ectopically expressed the DNA exonuclease TREX1 and the RNA:DNA hybrid-resolving nuclease RNASEH2B in MED12-depleted NP cells (Figure 7F)(46). Consistent with expectations, TREX1 overexpression selectively reduced the number of cytoplasmic RNA:DNA hybrids, whereas RNASEH2B overexpression significantly depleted these hybrid structures in both the nuclear and the cytoplasmic compartments (Figure 7G). Ectopic expression of both TREX1 and RNASEH2B substantially attenuated cytoplasmic ssDNA leakage in MED12-depleted NPCs (Figure 7H). Importantly, overexpression of TREX1 and RNase H1 alleviated the senescence phenotype induced by MED12 depletion, as evidenced by reduced expression of senescence-associated markers, diminished β-galactosidase activity, attenuated SASP activation, and restored cellular proliferative capacity (Figure 7, I and J, Supplemental Figure 8, A and B). These results demonstrate that MED12 deficiency triggers R-loop accumulation, which in turn activates the cGAS-STING axis-dependent inflammatory cascade.

PRMT2 deficiency promotes FBXO7-MED12-R-loop axis-dependent NPC senescence

We depleted endogenous FBXO7 and reconstituted it with either wild-type FBXO7 or the RF mutant in NP cells. Consistent with previous observations, PRMT2 knockdown induced senescence-associated phenotypes characterized by upregulated senescence-associated marker expression, elevated senescence-associated β-galactosidase activity, and genomic instability. Notably, reconstitution with the RF mutant conferred resistance to PRMT2 deficiency-driven senescence acquisition (Figure 8, A and B, Supplemental Figure 9A). Consistently, PRMT2 knockdown-induced activation of the cGAS–STING pathway was effectively blocked by reconstitution with the RF mutant (Supplemental Figure 9B). Furthermore, reconstituted expression of the FBXO7 RF mutant specifically ameliorated the PRMT2 knockdown-induced proinflammatory hypersecretory state, as evidenced by normalized cytokine expression profiles (Supplemental Figure 9C). Additionally, the PRMT2 knockdown-induced increase in R-loop formation and cytosolic ssDNA accumulation were significantly suppressed in RF mutant-reconstituted NPCs (Figure 8C, Supplemental Figure 9D). Collectively, these data demonstrated that the PRMT2-mediated methylation of FBXO7 at Arg504 suppressed R-loop formation and mitigated cGAS–STING axis-dependent inflammatory senescence in NPCs.

Next, we investigated the role of PRMT2 in FBXO7-mediated ubiquitin–proteasome degradation of MED12. Co-IP assays demonstrated that PRMT2 knockdown significantly increased the interaction between wild-type FBXO7 and MED12 in HEK293T cells. Conversely, PRMT2 depletion did not increase the interaction between the recombinantly expressed RF mutant and MED12 (Figure 8D). Moreover, PRMT2 knockdown significantly shortened the half-life of MED12 and increased its ubiquitination level in HEK293T cells transduced with recombinant wild-type FBXO7 plasmids, whereas these effects were abolished in cells transduced with RF mutant plasmids (Figure 8, E–G). Importantly, MED12 overexpression abrogated the PRMT2

knockdown-induced upregulation of senescence-associated markers (Figure 8H). Collectively, these findings support a model in which PRMT2-mediated methylation of FBXO7 impedes its interaction with MED12 and subsequent FBXO7-driven ubiquitin-dependent degradation of MED12, thereby suppressing pathological R-loop accumulation and ultimately inhibiting cGAS–STING axis-dependent proinflammatory cascades (Figure 8I).

EV-based MED12-overexpressing plasmid cargo alleviated NP cell senescence and IVDD progression

Finally, to explore the translational implications of this discovery, we utilized EVs for MED12 overexpression plasmid delivery. Compared with conventional vectors, EVs present inherent therapeutic advantages, including prolonged extracellular persistence, biological barrier penetrability, low immunogenicity, and abundant tissue availability(48-50). This approach strategically addresses the technical challenges posed by the substantial genomic footprint of the MED12 gene and current packaging limitations while capitalizing on the demonstrated capacity of EVs for intercellular cargo transfer. We hypothesize that MED12 plasmid-loaded EVs ameliorate NPC senescence and IVDD progression through the restoration of physiological MED12 protein levels. EVs were isolated from rat bone marrow mesenchymal stem cell (rBMSC) culture media via differential ultracentrifugation. Subsequently, MED12-overexpressing plasmids (MED12-EVs) and empty vector plasmids (vector-EVs) were loaded into EVs using optimized electroporation parameters (Figure 9A). Western blot analysis confirmed the presence of canonical EV biomarkers (CD63, CD9, and ALIX), confirming EV identity and purity (Figure 9B)(51). Agarose gel electrophoresis demonstrated efficient loading of MED12-overexpressing plasmids into EVs (Figure 9B). Nanoparticle tracking analysis (NTA)

and transmission electron microscopy (TEM) showed that MED12-EVs and vector-EVs exhibited irregular spheroidal morphologies with similar sizes (Figure 9, C and D). Notably, MED12-sEVs effectively rescued MED12 protein deficiency in degenerated NP cells, as quantified by western blot analysis (Figure 9E). Consistently, MED12-sEVs effectively alleviated senescence-associated phenotypes in degenerated NPCs, which was accompanied by reduced cGAS-STING axis-driven inflammatory cascade activation (Figure 9, F and G, Supplemental Figure 10, A and B). Next, we evaluated the therapeutic efficacy of MED12-EVs for IVDD in vivo. We established an IVDD model through caudal needle puncture in Sprague–Dawley rats via the intradiscal administration of PBS, Vector-EVs, or MED12-EVs (Figure 9A). In vivo fluorescence imaging of DiO-labelled EVs revealed their preferential accumulation at the central region of the intervertebral disc, demonstrating effective targeted delivery and confinement to the NP region without extravasation into surrounding tissues (Figure 9H). Furthermore, H&E staining of heart, liver, spleen, lung, and kidney showed no histological alterations or toxicity in the MED12-EVs group, supporting its biosafety (Supplemental Figure 10C). Radiological evaluation indicated that MED12-EVs attenuated puncture-induced DHI reduction and T2-weighted signal loss (Figure 9, I–K, O and P). Consistently, histological analysis demonstrated the therapeutic effects of MED12-EVs on coccygeal intervertebral discs. Compared with PBS and Vector-EV treatment, MED12-EV treatment markedly preserved the proteoglycan content and NP architecture (Figure 9, L and N). Furthermore, the specific localization of pronounced DiO-labelled green fluorescence within NP regions validated the targeted delivery efficiency of EVs, which was functionally correlated with the restoration of MED12 protein levels (Supplemental Figure 10D). To assess long-term retention and the sustained effect of MED12 overexpression, we performed DiO immunofluorescence and MED12

immunohistochemistry at 4 and 8 weeks post-injection, which revealed persistent EV-derived signal and maintained MED12 expression in the NP region (Supplemental Figure 10, E and F). Furthermore, MED12-EV treatment significantly reduced the number of γ-H2AX, p-p53, p21, and IL-1β positive cells (Figure 9M). In summary, we proposed and validated an EV-based MED12 restoration strategy to mitigate NP cell senescence and IVDD progression.

Discussion

In this study, we discovered that dysregulation of the methylation–ubiquitination -mediated destabilization of MED12 could promote abnormal R-loop accumulation, which represents a mechanism driving the inflammatory cascade in intervertebral disc degeneration. The loss of MED12 promoted R-loop formation, which activated cytoplasmic DNA sensing-related pathways and aberrantly induced cellular proinflammatory signalling pathways. Targeted restoration of MED12 suppressed senescence in NP cells and alleviated IVDD progression (Figure 10).

Multiple factors may contribute to the development of IVDD, and among these factors, cellular senescence has emerged as a critical risk factor associated with both the incidence and progression of IVDD (2, 4, 52). In-depth investigations of the pathogenesis of IVDD are important for developing targeted treatment strategies. Here, through comparative proteomic profiling of posttranslational events in degenerated versus normal intervertebral discs, we identified PRMT2 deficiency-mediated methylation–ubiquitination as an underlying mechanism driving disc inflammatory degeneration. Previous studies have demonstrated that PRMT2 deficiency promotes inflammatory responses through an NF-κB-dependent pathway(53). In this study, we revealed a mechanism whereby PRMT2 deficiency induced cytoplasmic self-DNA leakage, thereby triggering cGAS-STING-dependent inflammatory cascade activation. Our work identified PRMT2 as a pivotal safeguard against endogenous DAMP generation, diverging from previous models that focused on the direct interaction of PRMT2 with NF-κB subunits to suppress their transcriptional activity.

Intervertebral disc ageing is accompanied NP cell senescence(52, 54). Senescence limits the self-renewal ability of NP cells, and the limitations of self-renewal potential and the persistence of

environmental stresses ultimately lead to tissue inflammation and damage and the development of intervertebral disc degeneration(55-57). MED12 plays a crucial role in transcriptional regulation. It serves as a platform that recruits histone-modifying enzymes, coactivators, and transcription factors while simultaneously acting as a bridge connecting the Mediator complex with RNA polymerase II(34, 35, 58, 59). Intriguingly, the MED12-binding proteome we identified covered a notable portion of R-loop regulators. Coupled with its multifaceted role in transcriptional regulation, this finding prompted a rigorous investigation into how MED12 regulates R-loop homeostasis. Our findings demonstrate that MED12 deficiency drives R-loop accumulation, thereby activating the cGAS–STING axis to promote NPC senescence. Interestingly, previous studies showed that MED12 inhibition derepresses endogenous retrotransposons, which release cytosolic nucleic acids to activate both the type I interferon pathway and the NF-κB signalling pathway(60). Notably, prior work in other cell types has reported that MED12 loss can trigger senescence through alternative mechanisms, such as LIMK2-mediated dysregulation of actin cytoskeleton and cytokinesis failure, or through altered TGF-β signaling(61, 62). These observations indicate that the role of MED12 in senescence is highly context-dependent and varies across cell types. In the present study, we propose that MED12 deficiency promotes senescence primarily through dysregulation of R-loop accumulation and activation of the cGAS-STING- axis. Thus, our findings reveal a cell-type-specific mechanistic insight that extends the known functional repertoire of MED12 into disc degeneration. Future studies elucidating how MED12 scaffolds the assembly of functionally distinct protein complexes will be critical to reveal its role in maintaining transcriptional homeostasis and coordinating context-dependent biological programs, offering avenues to target MED12-driven regulatory networks in disease.

Several limitations of this study should be acknowledged. First, due to the difficulty in obtaining age-matched healthy adult disc tissues, we used pediatric scoliosis samples as controls, which introduces a potential age bias. Future studies with larger, properly age-stratified human cohorts are warranted to further dissect the contributions of aging versus degeneration. Second, our in vivo experiments were performed using a rat coccygeal puncture model, which offers excellent accessibility and reproducibility but does not fully replicate the biomechanical environment of the human lumbar spine. Future validation in a lumbar disc degeneration model would enhance translational relevance. Third, although our EV-based MED12 delivery showed efficacy in the rat model, substantial hurdles remain for clinical translation, including large-scale GMP-compliant production, potential immunogenicity, long-term safety, and regulatory approval. Ongoing efforts to improve EV targeting, reduce off-tissue effects, and optimize manufacturing will be essential before any clinical application can be envisioned.

In summary, our findings demonstrated that PRMT2 deficiency promoted MED12 degradation through methylation–ubiquitination crosstalk, driving R-loop/cGAS/STING axis-dependent inflammatory cascades. Furthermore, we engineered EVs encapsulating MED12-overexpressing plasmids, which effectively suppressed NPC senescence and alleviated IVDD progression, identifying MED12 as a potential therapeutic target for IVDD intervention.

Materials and Methods

Sex as a biological variable.

Our study incorporated clinical samples from both male and female donors. Our study exclusively examined female mice, as in our previous studies. It is unknown whether the findings are relevant for male mice.

Human NP samples

Human NP tissues were obtained from surgical procedures (lumbar vertebral fracture, idiopathic scoliosis or IVDD without hereditary diseases) with informed consent. Clinical medical records and radiographic MRI data were used to evaluate the degenerative grade of the human NP samples according to the Pfirrmann grading system(26). Donor information, including age, sex, clinical diagnosis and Pfirrmann grade, was anonymized and recorded. The NP samples were subjected to western blot analysis.

Cell culture and treatments

Human NP tissue samples were obtained from surgical disc specimens of patients who underwent lumbar vertebral fracture or idiopathic scoliosis(63). The tissues were minced and digested in 0.4% type II collagenase (Invitrogen, USA) dissolved in DMEM/F12 (Gibco) for 4 hours at 37°C with gentle agitation. The digested cells were centrifuged at 1200 rpm, rinsed twice with PBS, and then resuspended in complete medium containing DMEM/F12 supplemented with 10% foetal bovine serum (FBS; Gibco) and 1% penicillin–streptomycin (Gibco). The cells were cultured at 37°C in a humidified 5% CO_2 atmosphere. The HEK293T

cell line was purchased from the American Type Tissue Culture Collection (ATTC) and cultured in DMEM (Gibco, USA) supplemented with 10% FBS (Invitrogen, USA).

To establish an in vitro senescence model, NP cells were treated with 50 μM TBHP (Sigma-Aldrich, USA) for 5 consecutive days(64). To explore the effects of arginine methylation, 15 μM or 30 μM AdOx (MedChemExpress, USA), a PRMT inhibitor, was used to treat NP cells or HEK293T cells. To explore the dynamic stability of the MED12 protein, NP cells or HEK293T cells were treated with 100 μg/ml cycloheximide (CHX; MedChemExpress, USA) to inhibit de novo protein synthesis, and 10 μM MG132 (MedChemExpress, USA) to block proteasomal function was used to treat NP cells or HEK293T cells for 6 h, and 50 μM BafA1 (BafA1; MedChemExpress, USA was used to treat NP cells or HEK293T cells for 6 h) to block lysosomal function.

Animals

Three-month-old Sprague–Dawley rats (SD rats, female, 200 ± 20 g) were obtained from the Laboratory Animal Center of Huazhong University of Science and Technology.

Coccygeal IVD Needle Puncture IVDD Model

An IVDD model was established in three-month-old female Sprague–Dawley rats using a validated coccygeal needle puncture protocol. The rats were anaesthetized with 3% pentobarbital, and the tail skin was sterilized with iodophor. A 20-gauge needle was inserted perpendicularly into the NP region through the annulus fibrosus under aseptic conditions at the Co6-Co7 and Co7-Co8 coccygeal intervertebral discs. Rotate the needle 180° and hold for 10 seconds to induce annular injury(5, 65). Sham-operated controls underwent skin incision without disc puncture. Disc degeneration progression was assessed at 4 weeks postinjury via radiological

analysis (MRI, X-ray, and μCT), histological analysis (H & E and SO & FG staining) and IHC staining.

Statistical analysis

The data in this study are presented as the means ± standard deviations. The data were obtained from at least three independent experiments. Unpaired 2-tailed Student's t test was used to analyse the significance between two groups, whereas One-way ANOVA was used to analyse the significance among multiple groups. GraphPad Prism version 9.3.0 was used to analyse the data and statistical results.

Study approval:

The ethics for using volunteer samples was approved by the Ethics Committee of Tongji Medical College, Huazhong University of Science and Technology (No. S341). All animal experiments were approved by the Laboratory Animal Center of Huazhong University of Science and Technology (No. S2394).

Data and materials availability:

All individual values represented in graphs are provided in the Supporting Data Values file. The raw sequence data reported in this paper have been deposited in the Genome Sequence Archive (Genomics, Proteomics & Bioinformatics 2025) in National Genomics Data Center, China National Center for Bioinformation / Beijing Institute of Genomics, Chinese Academy of Sciences (GSA-Human: HRA017941). The mass spectrometry proteomics data have been

deposited to the ProteomeXchange Consortium via the iProX partner repository with the dataset identifier PXD0772788. Any other additional information is available from the corresponding authors upon reasonable request.

List of Supplementary Materials

Materials and Methods

FigureS1 to S10 for multiple supplementary figures

Table S1 to S12 for multiple supplementary tables

Author contributions:

Conceptualization: C. Y., H. L., Y. S.

Methodology: H. L., DCZ, ZD, XYL, RS

Investigation: H. L., D. Z., Z. D., X. L., R. S., D. W., X. Z., J. L., B. T., H. X., Z. O., J. W., W. K., B. W., X. F., K. W., Y. S., Y. D., S. P., Z. L.

Visualization: H. L., D. Z., Z. D., X. L., R. S.

Funding acquisition: C. Y., Y. S., H. L.

Project administration: H. L., D. Z., Z. D.

Supervision: C. Y., Y. S.

Writing – original draft: Y. S., H. L.

Writing – review & editing: C. Y., Y. S.

Funding:

• National Natural Science Foundation of China (82130072, 82072505 and 82472511)

• Natural Science Foundation of Hubei Province (2023CFA007)

• Shenzhen Science and Technology Program (SGDX20230116093544006)

• Open Research Project of Hubei Jiangxia Laboratory (2025JXKF014)

• Fundamental Research Funds for the Central Universities HUST (YCJJ20242118)

Acknowledgments:

We thank the Huazhong University of Science and Technology Analytical & Testing Center, Medical sub-center and Wuhan Center for Magnetic Resonance, Innovation Academy for Precision Measurement Science and Technology, Chinese Academy of Sciences, for technical support. The animal experiments in this work were also supported by Huazhong University of Science and Technology laboratory animal center. We thank the BioRender.com for providing some illustration in this manuscript.

Competing interests: The authors declare that they have no competing interests.

References and Notes

1. Binch ALA, Fitzgerald JC, Growney EA, and Barry F. Cell-based strategies for IVD repair: clinical progress and translational obstacles. *Nat Rev Rheumatol.* 2021;17(3):158-75.
2. Knezevic NN, Candido KD, Vlaeyen JWS, Van Zundert J, and Cohen SP. Low back pain. *Lancet.* 2021;398(10294):78-92.
3. Lyu FJ, Cui H, Pan H, Mc Cheung K, Cao X, Iatridis JC, et al. Painful intervertebral disc degeneration and inflammation: from laboratory evidence to clinical interventions. *Bone Res.* 2021;9(1):7.
4. Morris H, Gonçalves CF, Dudek M, Hoyland J, and Meng QJ. Tissue physiology revolving around the clock: circadian rhythms as exemplified by the intervertebral disc. *Ann Rheum Dis.* 2021;80(7):828-39.
5. Zhang W, Li G, Zhou X, Liang H, Tong B, Wu D, et al. Disassembly of the TRIM56-ATR complex promotes cytoDNA/cGAS/STING axis-dependent intervertebral disc inflammatory degeneration. *J Clin Invest.* 2024;134(6).
6. Zhao CQ, Wang LM, Jiang LS, and Dai LY. The cell biology of intervertebral disc aging and degeneration. *Ageing Res Rev.* 2007;6(3):247-61.
7. Burt KG, Kim MKM, Viola DC, Abraham AC, and Chahine NO. Nuclear factor κB overactivation in the intervertebral disc leads to macrophage recruitment and severe disc degeneration. *Sci Adv.* 2024;10(23):eadj3194.
8. Baker PJ, De Nardo D, Moghaddas F, Tran LS, Bachem A, Nguyen T, et al. Posttranslational Modification as a Critical Determinant of Cytoplasmic Innate Immune Recognition. *Physiol Rev.* 2017;97(3):1165-209.
9. Guccione E, and Richard S. The regulation, functions and clinical relevance of arginine methylation. *Nat Rev Mol Cell Biol.* 2019;20(10):642-57.
10. Barbour H, Nkwe NS, Estavoyer B, Messmer C, Gushul-Leclaire M, Villot R, et al. An inventory of crosstalk between ubiquitination and other post-translational modifications in orchestrating cellular processes. *iScience.* 2023;26(5):106276.
11. Vu LD, Gevaert K, and De Smet I. Protein Language: Post-Translational Modifications Talking to Each Other. *Trends Plant Sci.* 2018;23(12):1068-80.
12. Blanc RS, and Richard S. Arginine Methylation: The Coming of Age. *Mol Cell.* 2017;65(1):8-24.
13. Fan Y, Wang Y, Dan W, Zhang Y, Nie L, Ma Z, et al. PRMT5-mediated arginine methylation stabilizes GPX4 to suppress ferroptosis in cancer. *Nat Cell Biol.* 2025;27(4):641-53.
14. Wang YP, Zhou W, Wang J, Huang X, Zuo Y, Wang TS, et al. Arginine Methylation of MDH1 by CARM1 Inhibits Glutamine Metabolism and Suppresses Pancreatic Cancer. *Mol Cell.* 2016;64(4):673-87.
15. Zhu J, Li X, Cai X, Zha H, Zhou Z, Sun X, et al. Arginine monomethylation by PRMT7 controls MAVS-mediated antiviral innate immunity. *Mol Cell.* 2021;81(15):3171-86.e8.
16. Li S, Chen Y, Xie Y, Zhan H, Zeng Y, Zeng K, et al. FBXO7 Confers Mesenchymal Properties and Chemoresistance in Glioblastoma by Controlling Rbfox2-Mediated Alternative Splicing. *Adv Sci (Weinh).* 2023;10(33):e2303561.
17. Luo L, Wu X, Fan J, Dong L, Wang M, Zeng Y, et al. FBXO7 ubiquitinates PRMT1 to suppress serine synthesis and tumor growth in hepatocellular carcinoma. *Nat Commun.* 2024;15(1):4790.
18. Arce MM, Umhoefer JM, Arang N, Kasinathan S, Freimer JW, Steinhart Z, et al. Central control of dynamic gene circuits governs T cell rest and activation. *Nature.* 2025;637(8047):930-9.
19. Chao TC, Chen SF, Kim HJ, Tang HC, Tseng HC, Xu A, et al. Structural basis of the human transcriptional Mediator regulated by its dissociable kinase module. *Mol Cell.* 2024;84(20):3932-49.e10.
20. Freitas KA, Belk JA, Sotillo E, Quinn PJ, Ramello MC, Malipatlolla M, et al. Enhanced T cell effector activity by targeting the Mediator kinase module. *Science.* 2022;378(6620):eabn5647.
21. Maia-Silva D, Cunniff PJ, Schier AC, Skopelitis D, Trousdell MC, Moresco P, et al. Interaction between MED12 and ΔNp63 activates basal identity in pancreatic ductal adenocarcinoma. *Nat Genet.* 2024;56(7):1377-85.
22. Bartel RL, and Borchardt RT. Effects of adenosine dialdehyde on S-adenosylhomocysteine hydrolase and S-adenosylmethionine-dependent transmethylations in mouse L929 cells. *Mol Pharmacol.* 1984;25(3):418-24.
23. Campbell M, Chang PC, Huerta S, Izumiya C, Davis R, Tepper CG, et al. Protein arginine methyltransferase 1-directed methylation of Kaposi sarcoma-associated herpesvirus latency-associated nuclear antigen. *J Biol Chem.* 2012;287(8):5806-18.

24. McBride AE, Cook JT, Stemmler EA, Rutledge KL, McGrath KA, and Rubens JA. Arginine methylation of yeast mRNA-binding protein Npl3 directly affects its function, nuclear export, and intranuclear protein interactions. *J Biol Chem.* 2005;280(35):30888-98.
25. Gorgoulis V, Adams PD, Alimonti A, Bennett DC, Bischof O, Bishop C, et al. Cellular Senescence: Defining a Path Forward. *Cell.* 2019;179(4):813-27.
26. Pfirrmann CW, Metzdorf A, Zanetti M, Hodler J, and Boos N. Magnetic resonance classification of lumbar intervertebral disc degeneration. *Spine (Phila Pa 1976).* 2001;26(17):1873-8.
27. Rutges JP, Duit RA, Kummer JA, Bekkers JE, Oner FC, Castelein RM, et al. A validated new histological classification for intervertebral disc degeneration. *Osteoarthritis Cartilage.* 2013;21(12):2039-47.
28. Espejo A, Côté J, Bednarek A, Richard S, and Bedford MT. A protein-domain microarray identifies novel protein-protein interactions. *Biochem J.* 2002;367(Pt 3):697-702.
29. Ren R, Mayer BJ, Cicchetti P, and Baltimore D. Identification of a ten-amino acid proline-rich SH3 binding site. *Science.* 1993;259(5098):1157-61.
30. Liu L, Lin B, Yin S, Ball LE, Delaney JR, Long DT, et al. Arginine methylation of BRD4 by PRMT2/4 governs transcription and DNA repair. *Sci Adv.* 2022;8(49):eadd8928.
31. Jackson PK, and Eldridge AG. The SCF ubiquitin ligase: an extended look. *Mol Cell.* 2002;9(5):923-5.
32. Nelson DE, Randle SJ, and Laman H. Beyond ubiquitination: the atypical functions of Fbxo7 and other F-box proteins. *Open Biol.* 2013;3(10):130131.
33. Dannappel MV, Zhu D, Sun X, Chua HK, Poppelaars M, Suehiro M, et al. CDK8 and CDK19 regulate intestinal differentiation and homeostasis via the chromatin remodeling complex SWI/SNF. *J Clin Invest.* 2022;132(20).
34. Aranda-Orgilles B, Saldaña-Meyer R, Wang E, Trompouki E, Fassl A, Lau S, et al. MED12 Regulates HSC-Specific Enhancers Independently of Mediator Kinase Activity to Control Hematopoiesis. *Cell Stem Cell.* 2016;19(6):784-99.
35. Gao WW, Xiao RQ, Zhang WJ, Hu YR, Peng BL, Li WJ, et al. JMJD6 Licenses ERα-Dependent Enhancer and Coding Gene Activation by Modulating the Recruitment of the CARM1/MED12 Co-activator Complex. *Mol Cell.* 2018;70(2):340-57.e8.
36. Buetow L, and Huang DT. Structural insights into the catalysis and regulation of E3 ubiquitin ligases. *Nat Rev Mol Cell Biol.* 2016;17(10):626-42.
37. Wang C, Tan X, Tang D, Gou Y, Han C, Ning W, et al. GPS-Uber: a hybrid-learning framework for prediction of general and E3-specific lysine ubiquitination sites. *Brief Bioinform.* 2022;23(2).
38. De Cecco M, Ito T, Petrashen AP, Elias AE, Skvir NJ, Criscione SW, et al. L1 drives IFN in senescent cells and promotes age-associated inflammation. *Nature.* 2019;566(7742):73-8.
39. Ivanov A, Pawlikowski J, Manoharan I, van Tuyn J, Nelson DM, Rai TS, et al. Lysosome-mediated processing of chromatin in senescence. *J Cell Biol.* 2013;202(1):129-43.
40. Dou Z, Xu C, Donahue G, Shimi T, Pan JA, Zhu J, et al. Autophagy mediates degradation of nuclear lamina. *Nature.* 2015;527(7576):105-9.
41. Chatzidoukaki O, Stratigi K, Goulielmaki E, Niotis G, Akalestou-Clocher A, Gkirtzimanaki K, et al. R-loops trigger the release of cytoplasmic ssDNAs leading to chronic inflammation upon DNA damage. *Sci Adv.* 2021;7(47):eabj5769.
42. De Silva NS, Siewiera J, Alkhoury C, Nader GPF, Nadalin F, de Azevedo K, et al. Nuclear envelope disruption triggers hallmarks of aging in lung alveolar macrophages. *Nat Aging.* 2023;3(10):1251-68.
43. Lin R, Zhong X, Zhou Y, Geng H, Hu Q, Huang Z, et al. R-loopBase: a knowledgebase for genome-wide R-loop formation and regulation. *Nucleic Acids Res.* 2022;50(D1):D303-d15.
44. Ren X, Liu Q, Zhou P, Zhou T, Wang D, Mei Q, et al. DHX9 maintains epithelial homeostasis by restraining R-loop-mediated genomic instability in intestinal stem cells. *Nat Commun.* 2024;15(1):3080.
45. Weinreb JT, Ghazale N, Pradhan K, Gupta V, Potts KS, Tricomi B, et al. Excessive R-loops trigger an inflammatory cascade leading to increased HSPC production. *Dev Cell.* 2021;56(5):627-40.e5.
46. Maxwell MB, Hom-Tedla MS, Yi J, Li S, Rivera SA, Yu J, et al. ARID1A suppresses R-loop-mediated STING-type I interferon pathway activation of anti-tumor immunity. *Cell.* 2024;187(13):3390-408.e19.
47. Smolka JA, Sanz LA, Hartono SR, and Chédin F. Recognition of RNA by the S9.6 antibody creates pervasive artifacts when imaging RNA:DNA hybrids. *J Cell Biol.* 2021;220(6).
48. Kao CY, and Papoutsakis ET. Engineering human megakaryocytic microparticles for targeted delivery of nucleic acids to hematopoietic stem and progenitor cells. *Sci Adv.* 2018;4(11):eaau6762.
49. Cheng L, and Hill AF. Therapeutically harnessing extracellular vesicles. *Nat Rev Drug Discov.* 2022;21(5):379-99.

50. Lu X, Kong X, Wu H, Hao J, Li S, Gu Z, et al. UBE2M-mediated neddylation of TRIM21 regulates obesity-induced inflammation and metabolic disorders. *Cell Metab.* 2023;35(8):1390-405.e8.
51. van Niel G, D'Angelo G, and Raposo G. Shedding light on the cell biology of extracellular vesicles. *Nat Rev Mol Cell Biol.* 2018;19(4):213-28.
52. Novais EJ, Tran VA, Johnston SN, Darris KR, Roupas AJ, Sessions GA, et al. Long-term treatment with senolytic drugs Dasatinib and Quercetin ameliorates age-dependent intervertebral disc degeneration in mice. *Nat Commun.* 2021;12(1):5213.
53. Sauter C, Morin T, Guidez F, Simonet J, Fournier C, Row C, et al. Protein arginine methyltransferase 2 controls inflammatory signaling in acute myeloid leukemia. *Commun Biol.* 2024;7(1):753.
54. Sakai D, Nakamura Y, Nakai T, Mishima T, Kato S, Grad S, et al. Exhaustion of nucleus pulposus progenitor cells with ageing and degeneration of the intervertebral disc. *Nat Commun.* 2012;3:1264.
55. Wan M, Gray-Gaillard EF, and Elisseeff JH. Cellular senescence in musculoskeletal homeostasis, diseases, and regeneration. *Bone Res.* 2021;9(1):41.
56. Chen F, Lei L, Chen S, Zhao Z, Huang Y, Jiang G, et al. Serglycin secreted by late-stage nucleus pulposus cells is a biomarker of intervertebral disc degeneration. *Nat Commun.* 2024;15(1):47.
57. Ramteke P, Watson B, Toci M, Tran VA, Johnston S, Tsingas M, et al. Sirt6 deficiency promotes senescence and age-associated intervertebral disc degeneration in mice. *Bone Res.* 2025;13(1):50.
58. Sooraj D, Sun C, Doan A, Garama DJ, Dannappel MV, Zhu D, et al. MED12 and BRD4 cooperate to sustain cancer growth upon loss of mediator kinase. *Mol Cell.* 2022;82(1):123-39.e7.
59. Enane FO, Shuen WH, Gu X, Quteba E, Przychodzen B, Makishima H, et al. GATA4 loss of function in liver cancer impedes precursor to hepatocyte transition. *J Clin Invest.* 2017;127(9):3527-42.
60. Tang Y, Tang S, Yang W, Zhang Z, Wang T, Wu Y, et al. MED12 loss activates endogenous retroelements to sensitise immunotherapy in pancreatic cancer. *Gut.* 2024;73(12):1999-2011.
61. Xu M, Wang F, Li G, Wang X, Fang X, Jin H, et al. MED12 exerts an emerging role in actin-mediated cytokinesis via LIMK2/cofilin pathway in NSCLC. *Mol Cancer.* 2019;18(1):93.
62. Huang S, Hölzel M, Knijnenburg T, Schlicker A, Roepman P, McDermott U, et al. MED12 controls the response to multiple cancer drugs through regulation of TGF-β receptor signaling. *Cell.* 2012;151(5):937-50.
63. Cheng X, Zhang L, Zhang K, Zhang G, Hu Y, Sun X, et al. Circular RNA VMA21 protects against intervertebral disc degeneration through targeting miR-200c and X linked inhibitor-of-apoptosis protein. *Ann Rheum Dis.* 2018;77(5):770-9.
64. Jing Y, Jiang X, Ji Q, Wu Z, Wang W, Liu Z, et al. Genome-wide CRISPR activation screening in senescent cells reveals SOX5 as a driver and therapeutic target of rejuvenation. *Cell Stem Cell.* 2023;30(11):1452-71.e10.
65. Chen S, Wu X, Lai Y, Chen D, Bai X, Liu S, et al. Kindlin-2 inhibits Nlrp3 inflammasome activation in nucleus pulposus to maintain homeostasis of the intervertebral disc. *Bone Res.* 2022;10(1):5.

Figures

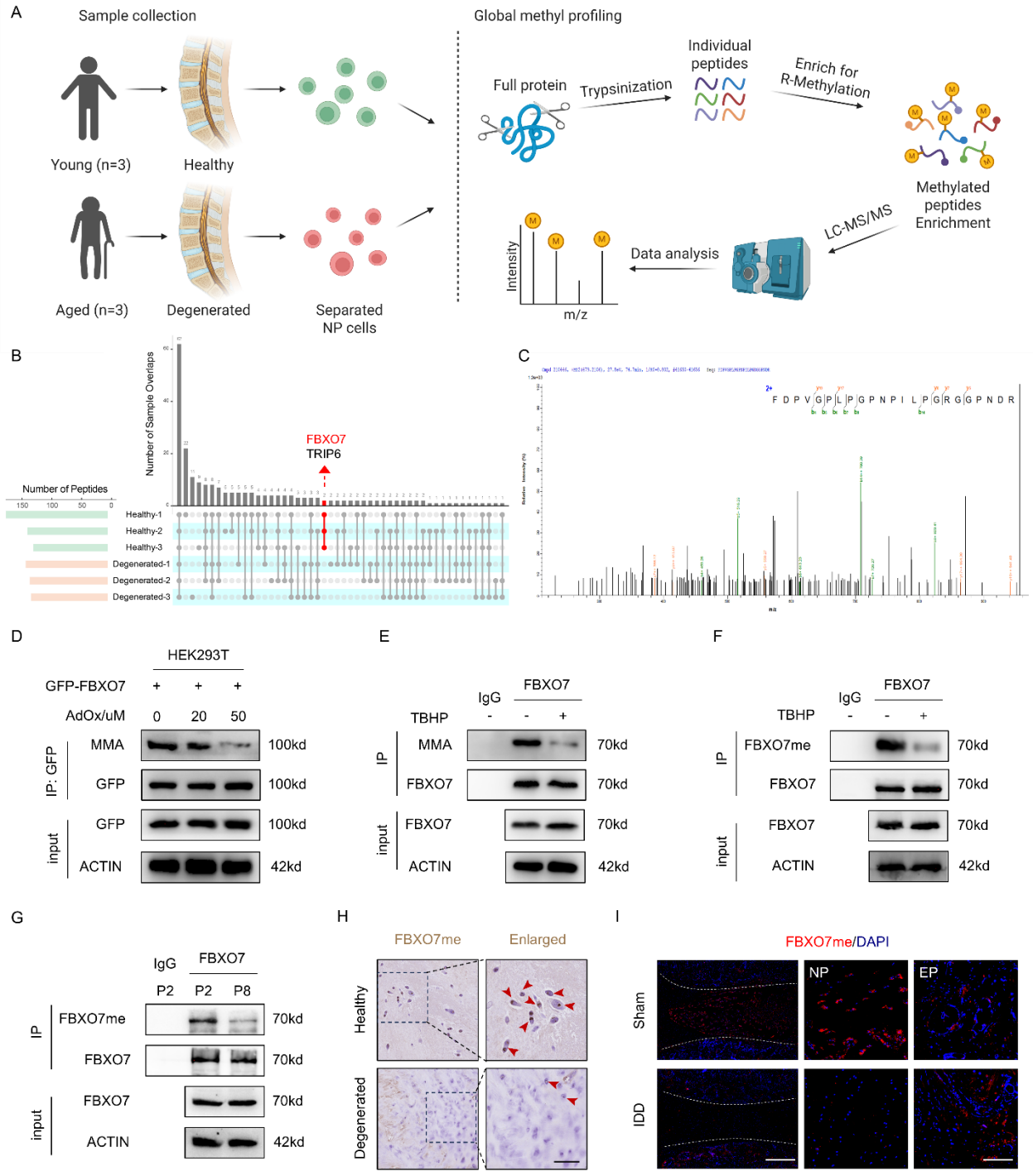

Figure 1. FBXO7 methylation is downregulated in IVDD.

(**A**) Schematic representation of the experimental design to quantify the arginine methyl proteome in IVDD. (**B**) Upset plot indicate the presence of arginine methylated peptides identified in each sample. (**C**) LC-MS/MS spectrum of the tryptic peptide FDPVGPLPGPNPILPGRGGPNDR identified a monomethylated residue at R504. (**D**) Methyltransferase inhibitors decrease FBXO7 methylation. GFP-tagged FBXO7 was expressed in HEK293cells, followed by treatment with increasing concentrations of methyltransferase inhibitors, AdOx. (**E**) Co-IP analysis of methylated FBXO7 in NPCs with the indicated treatment. (**F**) Co-IP analysis of FBXO7-R504me in NPCs with the indicated treatment. (**G**) Co-IP analysis of FBXO7-R504me in P2 and P8 NPCs. (**H**) IHC of the FBXO7-R504me in human NP tissue (Scale bar: 100μm). (**I**) IF staining of FBXO7-R504me in coccygeal vertebrae from rats with the indicated treatment (Scale bar: 1 mm, 250 μm). At least 3 independent experiments were performed.

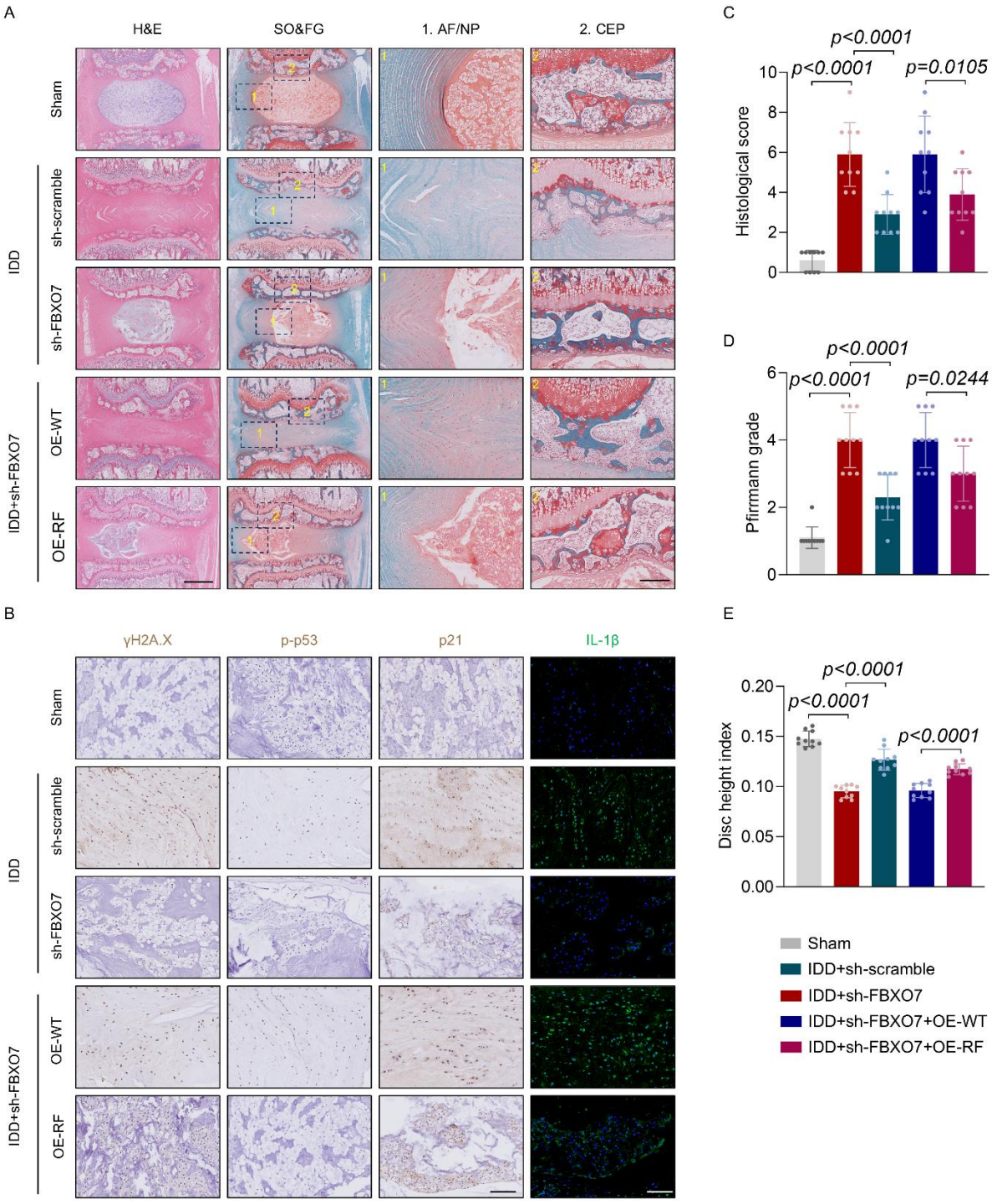

788

789 **Figure 2. FBXO7 methylation deficiency promotes NP cell senescence and IVDD**

790 **progression.** (**A**) H&E staining and SO&FG staining of coccygeal vertebrae from rats with the

791 indicated treatment (Scale bar: 1mm, 250 μm). (**B**) IHC staining and IF staining of p-p53,

γH2A.X, p21 and IL-1β in rat coccygeal IVDs. (Scale bar: 100 μm). (**C**) Histological score (n = 10), (**D**) Pfirrmann degenerative grades (n = 10) and (**E**) disc height index (n = 10) of rat coccygeal IVDs. One-way ANOVA (**C**, **D**, **E**) was used to performed, and data are represented as mean ± SD. At least 3 independent experiments were performed.

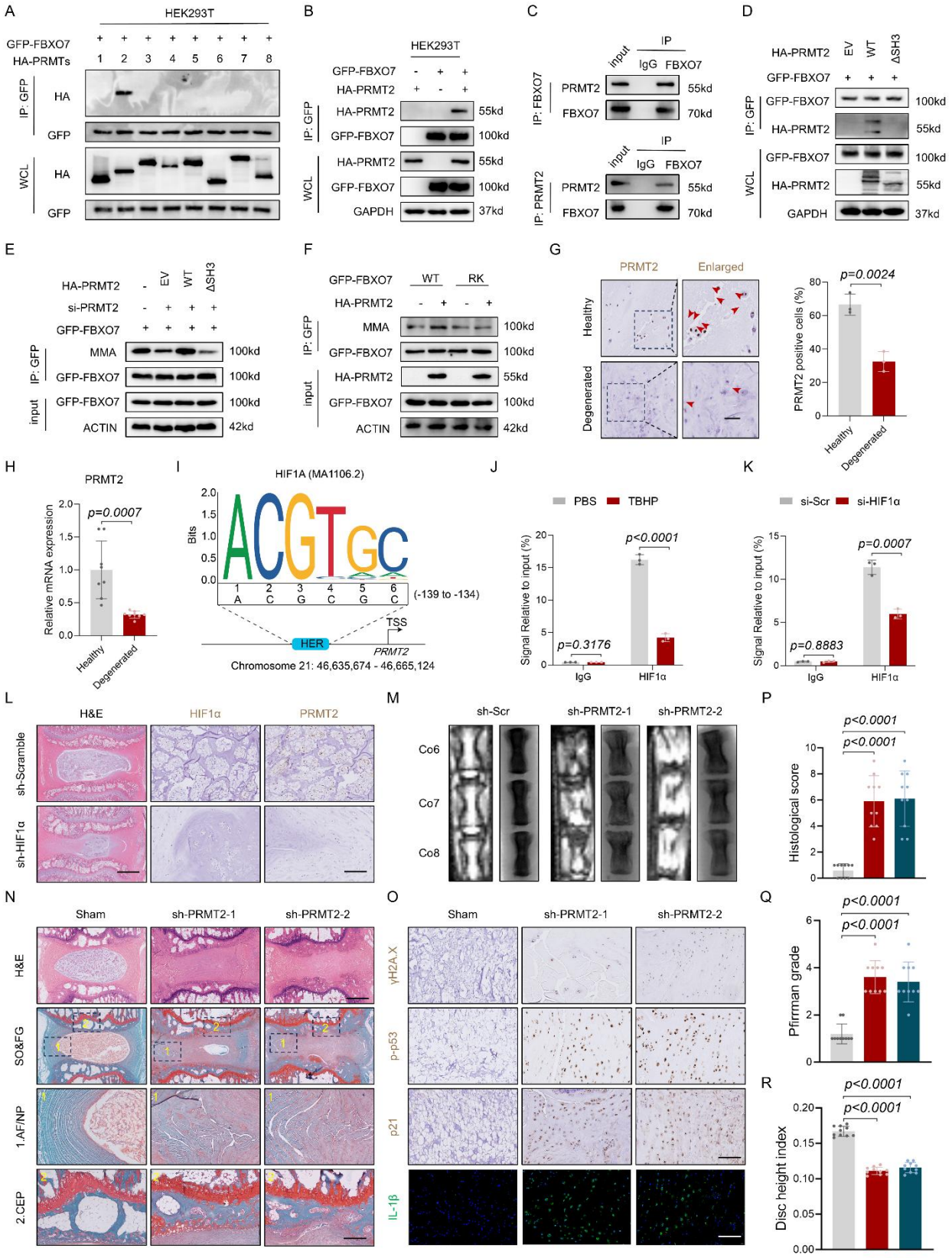
A
HEK293T
GFP-FBXO7
HA-PRMTs
1 2 3 4 5 6 7 8
IP: GFP
HA
GFP
WCL
HA
GFP
B
HEK293T
GFP-FBXO7
HA-PRMT2
IP: GFP
HA-PRMT2
GFP-FBXO7
WCL
HA-PRMT2
GFP-FBXO7
GAPDH
55kd
100kd
55kd
100kd
37kd
C
input
IP
IgG
FBXO7
IP: FBXO7
PRMT2
FBXO7
IP: PRMT2
PRMT2
FBXO7
55kd
70kd
D
HA-PRMT2
EV
WT
ΔSH3
GFP-FBXO7
IP: GFP
GFP-FBXO7
HA-PRMT2
WCL
GFP-FBXO7
HA-PRMT2
GAPDH
100kd
55kd
100kd
55kd
37kd
E
HA-PRMT2
si-PRMT2
GFP-FBXO7
EV
WT
ΔSH3
IP: GFP
MMA
GFP-FBXO7
input
GFP-FBXO7
ACTIN
100kd
100kd
100kd
42kd
F
GFP-FBXO7
WT
RK
HA-PRMT2
IP: GFP
MMA
GFP-FBXO7
input
HA-PRMT2
GFP-FBXO7
ACTIN
100kd
100kd
55kd
100kd
42kd
G
PRMT2
Enlarged
Healthy
Degenerated
p=0.0024
PRMT2 positive cells (%)
Healthy
Degenerated
H
PRMT2
p=0.0007
Relative mRNA expression
Healthy
Degenerated
I
HIF1A (MA1106.2)
Bits
(-139 to -134)
HER
TSS
PRMT2
Chromosome 21: 46,635,674 - 46,665,124
J
PBS
TBHP
p<0.0001
p=0.3176
Signal Relative to input (%)
IgG
HIF1α
K
si-Scr
si-HIF1α
p=0.0007
p=0.8883
Signal Relative to input (%)
IgG
HIF1α
L
H&E
HIF1α
PRMT2
sh-Scramble
sh-HIF1α
M
sh-Scr
sh-PRMT2-1
sh-PRMT2-2
Co6
Co7
Co8
P
p<0.0001
p<0.0001
Histological score
Q
p<0.0001
p<0.0001
Pfirrman grade
R
p<0.0001
p<0.0001
Disc height index
N
Sham
sh-PRMT2-1
sh-PRMT2-2
H&E
SO&FG
1.AF/NP
2.CEP
O
Sham
sh-PRMT2-1
sh-PRMT2-2
γH2A.X
p-p53
p21
IL-1β

797

Figure 3. Loss of PRMT2-mediated FBXO7 Arg504 methylation promoted NP cell senescence and IVDD progression

(**A**) Proteins were immunoprecipitated using GFP antibody and analyzed by western blotting in HEK293T cells transfected with indicated constructs. (**B**) Exogenous Co-IP analysis of the interaction of FBXO7 with PRMT2 in HEK293T cells (**C**) Endogenous Co-IP analysis of the interaction of FBXO7 with PRMT2 in NPCs. (**D**) Proteins were immunoprecipitated using GFP antibody and analyzed by western blotting in HEK293T cells transfected with indicated constructs. (**E**) Co-IP analysis of methylated FBXO7 in PRMT2-silenced HEK293T cells (**F**) Co-IP analysis of methylated FBXO7 in HEK293T cells transfected with indicated constructs. (**G**) IHC of the PRMT2 in human NP tissue (Scale bar: 100μm). (**H**) mRNA expression analysis of PRMT2 in human NP tissue by RT-qPCR. (**I**) Schematic diagram shows that the base sequence represents the consensus HIF1α-binding motif. (**J**) ChIP-PCR analysis of the enrichment of HIF1α in the PRMT2 promoter in NPCs with the indicated treatment. (**K**) ChIP-PCR analysis of the enrichment of HIF1α in the PRMT2 promoter in NPCs with HIF1α silencing. (**L**) H&E staining and IHC staining coccygeal vertebrae from rats with the indicated treatment (Scale bar: 1 mm, 100μm). (**M**) Representative X-ray and MRI images of coccygeal vertebrae from rats with the indicated treatment. (**N**) H&E staining and SO&FG staining of coccygeal vertebrae from rats with the indicated treatment (Scale bar: 1 mm, 250 μm). (**O**) IHC staining and IF staining of p-p53, γH2A.X, p21 and IL-1β in rat coccygeal IVDs (Scale bar: 100 μm). (**P**) Histological score, (**Q**) Pfirrmann degenerative grades and (**R**) disc height index of rat coccygeal IVDs. Unpair students' t test (**G, H, J, K**) were used to performed, one-way ANOVA (**P**, **Q, R**) was used to performed, and data are represented as mean ± SD. At least 3 independent experiments were performed.

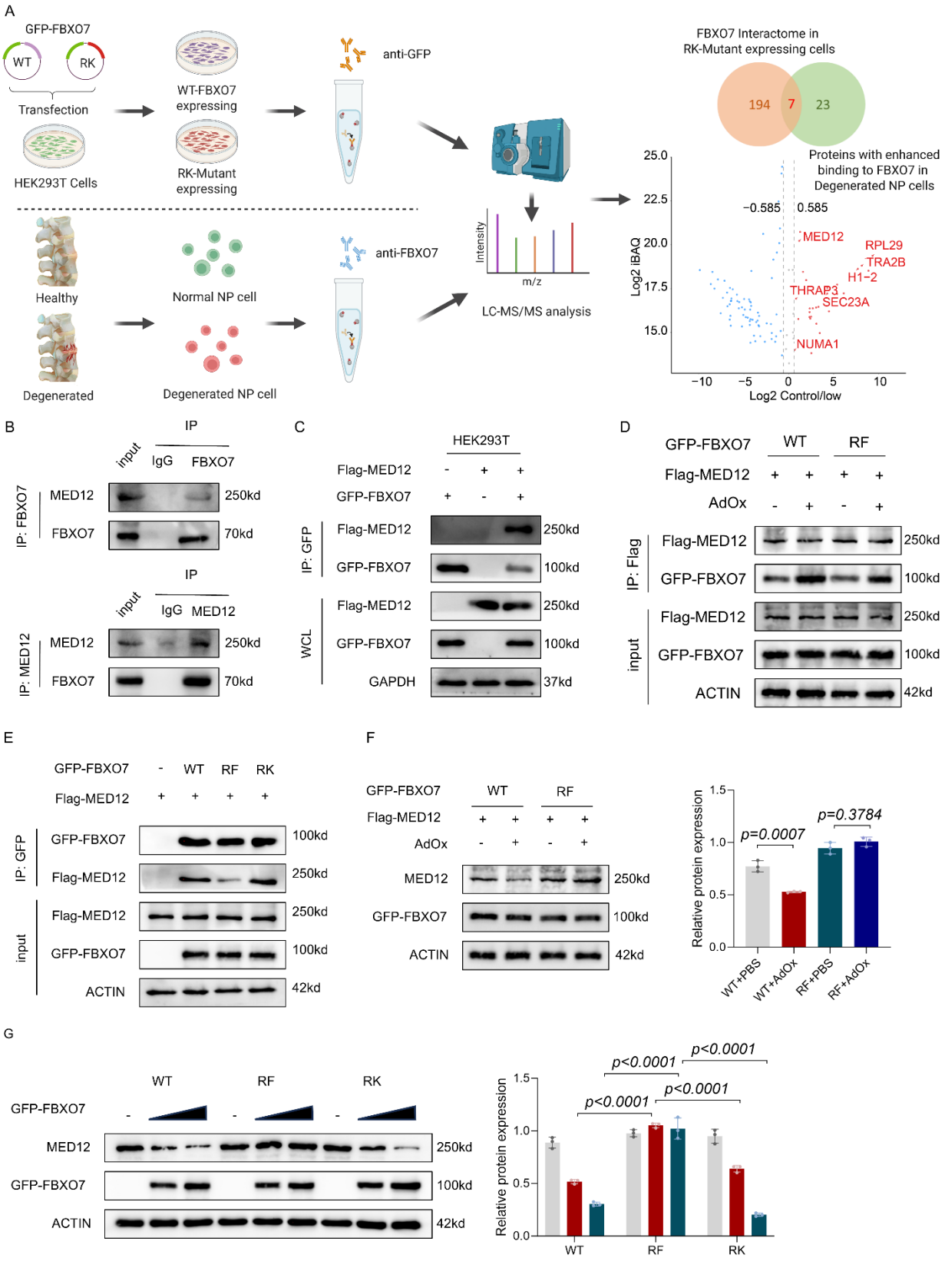
A
GFP-FBXO7
WT
RK
Transfection
HEK293T Cells
WT-FBXO7 expressing
RK-Mutant expressing
anti-GFP
anti-FBXO7
Healthy
Degenerated
Normal NP cell
Degenerated NP cell
LC-MS/MS analysis
Intensity
m/z
FBXO7 Interactome in RK-Mutant expressing cells
194
7
23
Proteins with enhanced binding to FBXO7 in Degenerated NP cells
−0.585
0.585
MED12
RPL29
TRA2B
H1-2
THRAP3
SEC23A
NUMA1
Log2 IBAQ
Log2 Control/low
B
IP
input
IgG
FBXO7
IP: FBXO7
MED12
FBXO7
250kd
70kd
IP
input
IgG
MED12
IP: MED12
MED12
FBXO7
250kd
70kd
C
HEK293T
Flag-MED12
GFP-FBXO7
IP: GFP
WCL
Flag-MED12
GFP-FBXO7
GAPDH
250kd
100kd
37kd
D
GFP-FBXO7
WT
RF
Flag-MED12
AdOx
IP: Flag
input
Flag-MED12
GFP-FBXO7
ACTIN
250kd
100kd
42kd
E
GFP-FBXO7
WT
RF
RK
Flag-MED12
IP: GFP
input
GFP-FBXO7
Flag-MED12
ACTIN
100kd
250kd
42kd
F
GFP-FBXO7
WT
RF
Flag-MED12
AdOx
MED12
GFP-FBXO7
ACTIN
250kd
100kd
42kd
Relative protein expression
p=0.0007
p=0.3784
WT+PBS
WT+AdOx
RF+PBS
RF+AdOx
G
WT
RF
RK
GFP-FBXO7
MED12
GFP-FBXO7
ACTIN
250kd
100kd
42kd
Relative protein expression
p<0.0001
p<0.0001
p<0.0001
p<0.0001
WT
RF
RK

821

Figure 4. FBXO7 Arg504 methylation prevents FBXO7-mediated MED12 recruitment and destabilization

(**A**) Schematic workflow showing IP-MS performed to identify FBXO7-interacting proteins in NP cells and HEK293T cells. (**B**) Endogenous Co-IP analysis of the interaction of FBXO7 with MED12 in NPCs. (**C**) Exogenous Co-IP analysis of the interaction of FBXO7 with MED12 in HEK293T cells cotransfected with GFP-FBXO7 and Flag-MED12. (**D**) Co-IP analysis of the interaction of FBXO7 with MED12 in in HEK293T cells cotransfected with Flag-MED12 and GFP-FBXO7 (wild-type, RF mutants) with the indicated treatment. (**E**) Co-IP analysis of the interaction of FBXO7 with MED12 in HEK293T cells cotransfected with Flag-MED12 and GFP-FBXO7 (wild-type, RK mutants and RFmutants). (**F**) Protein level analysis of MED12 in HEK293T cells cotransfected with Flag-MED12 and GFP-FBXO7 (wild-type, RF mutants) with the indicated treatment by western blot. (**G**) Protein level analysis of MED12 in NPCs overexpressed FBXO7 by western blot. One-way ANOVA (**F**, **G**) was used to performed, and data are represented as mean ± SD. At least 3 independent experiments were performed.

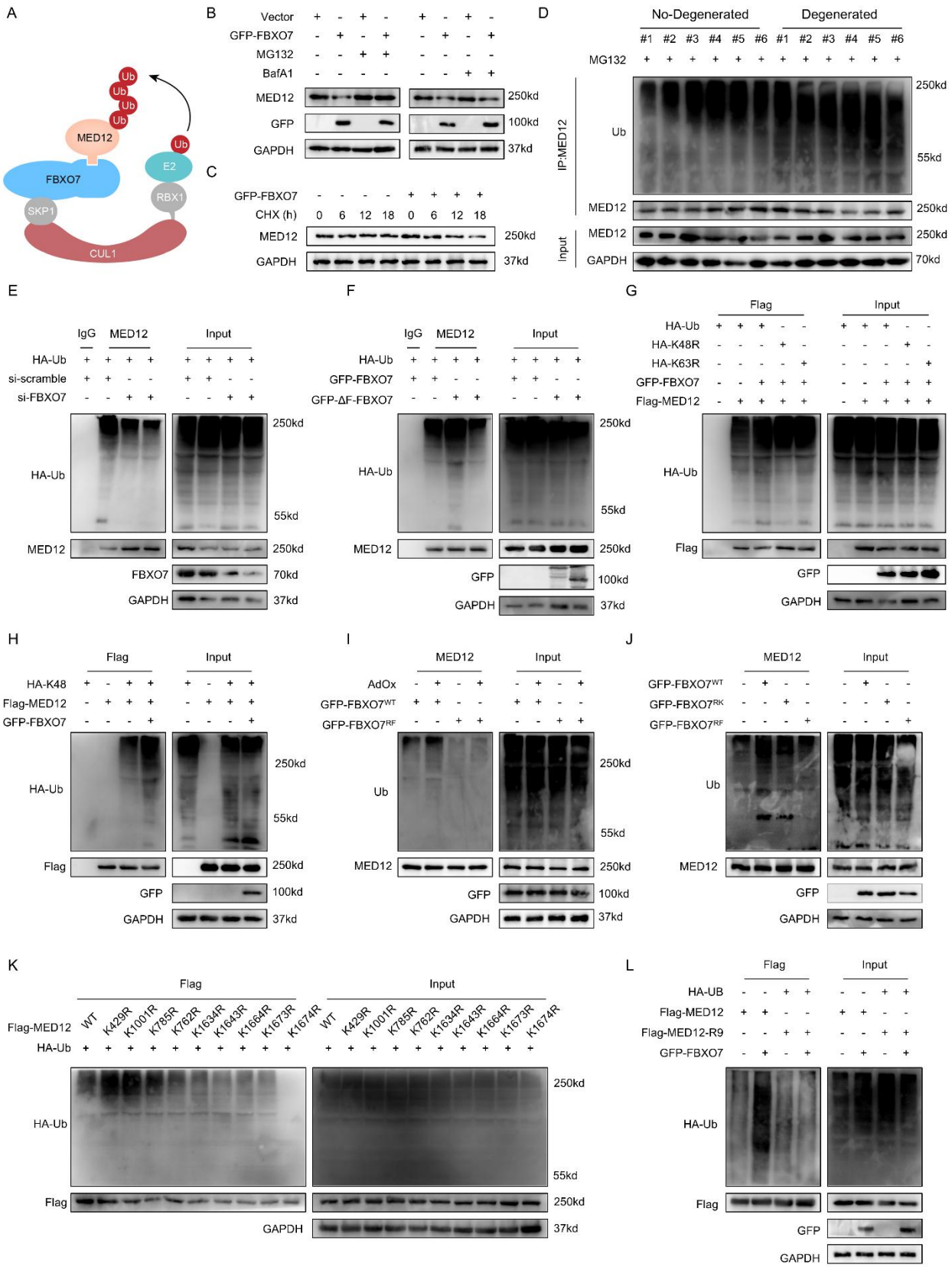
A
Ub
MED12
FBXO7
E2
RBX1
SKP1
CUL1
B
Vector
GFP-FBXO7
MG132
BafA1
MED12
GFP
GAPDH
250kd
100kd
37kd
C
GFP-FBXO7
CHX (h)
0 6 12 18 0 6 12 18
MED12
GAPDH
250kd
37kd
D
No-Degenerated
Degenerated
#1 #2 #3 #4 #5 #6 #1 #2 #3 #4 #5 #6
MG132
IP:MED12
Ub
MED12
Input
MED12
GAPDH
250kd
55kd
70kd
E
IgG
MED12
Input
HA-Ub
si-scramble
si-FBXO7
HA-Ub
MED12
FBXO7
GAPDH
250kd
55kd
70kd
37kd
F
IgG
MED12
Input
HA-Ub
GFP-FBXO7
GFP-ΔF-FBXO7
HA-Ub
MED12
GFP
GAPDH
250kd
55kd
100kd
37kd
G
Flag
Input
HA-Ub
HA-K48R
HA-K63R
GFP-FBXO7
Flag-MED12
HA-Ub
Flag
GFP
GAPDH
H
Flag
Input
HA-K48
Flag-MED12
GFP-FBXO7
HA-Ub
Flag
GFP
GAPDH
250kd
55kd
100kd
37kd
I
MED12
Input
AdOx
GFP-FBXO7WT
GFP-FBXO7RF
Ub
MED12
GFP
GAPDH
250kd
55kd
100kd
37kd
J
MED12
Input
GFP-FBXO7WT
GFP-FBXO7RK
GFP-FBXO7RF
Ub
MED12
GFP
GAPDH
K
Flag
Input
Flag-MED12
WT K429R K1001R K785R K762R K1634R K1643R K1664R K1673R K1674R
HA-Ub
HA-Ub
Flag
GAPDH
250kd
55kd
37kd
L
Flag
Input
HA-UB
Flag-MED12
Flag-MED12-R9
GFP-FBXO7
HA-Ub
Flag
GFP
GAPDH

836

Figure 5. FBXO7 Arg504 methylation impedes FBXO7-mediated K48-linked ubiquitination of MED12

(**A**) A model of MED12 protein polyubiquitination by the FBXO7 E3 ligase complex. (**B** and **C**) Protein level analysis of MED12 in NP cells overexpressed FBXO7 with indicated treatment (**D**) Half-life analysis of MED12 protein in NPCs with or without FBXO7 overexpression. (**E**) Co-IP analysis of MED12 ubiquitination in human sample (**F**) Co-IP analysis of endogenous MED12 ubiquitination in NPCs treated with si-FBXO7. (**G**) Co-IP analysis of endogenous MED12 ubiquitination in NPCs overexpressed with wild-type FBXO7 or F-box domain-deleted ΔF-FBXO7 mutant. (**H**) Co-IP analysis of exogenous MED12 ubiquitination in HEK293T cells transfected with various combinations of plasmids. (**I**) Co-IP analysis of exogenous MED12 ubiquitination in HEK293T cells transfected with various combinations of plasmids. (**J**) Co-IP analysis of endogenous MED12 ubiquitination in NPCs transfected with wild-type FBXO7 or FBXO7 RF mutant with the indicated treatment. (**K**) Co-IP analysis of endogenous MED12 ubiquitination in NPCs overexpressed with FBXO7 (wild-type, RF mutants, RK mutants) with the indicated treatment. (**L**) Co-IP analysis of exogenous MED12 ubiquitination of wide-type MED12 and mutants in HEK293T cells (**M**) Co-IP analysis of exogenous MED12 ubiquitination wide-type MED12 and K1674R mutants in HEK293T cells. At least 3 independent experiments were performed.

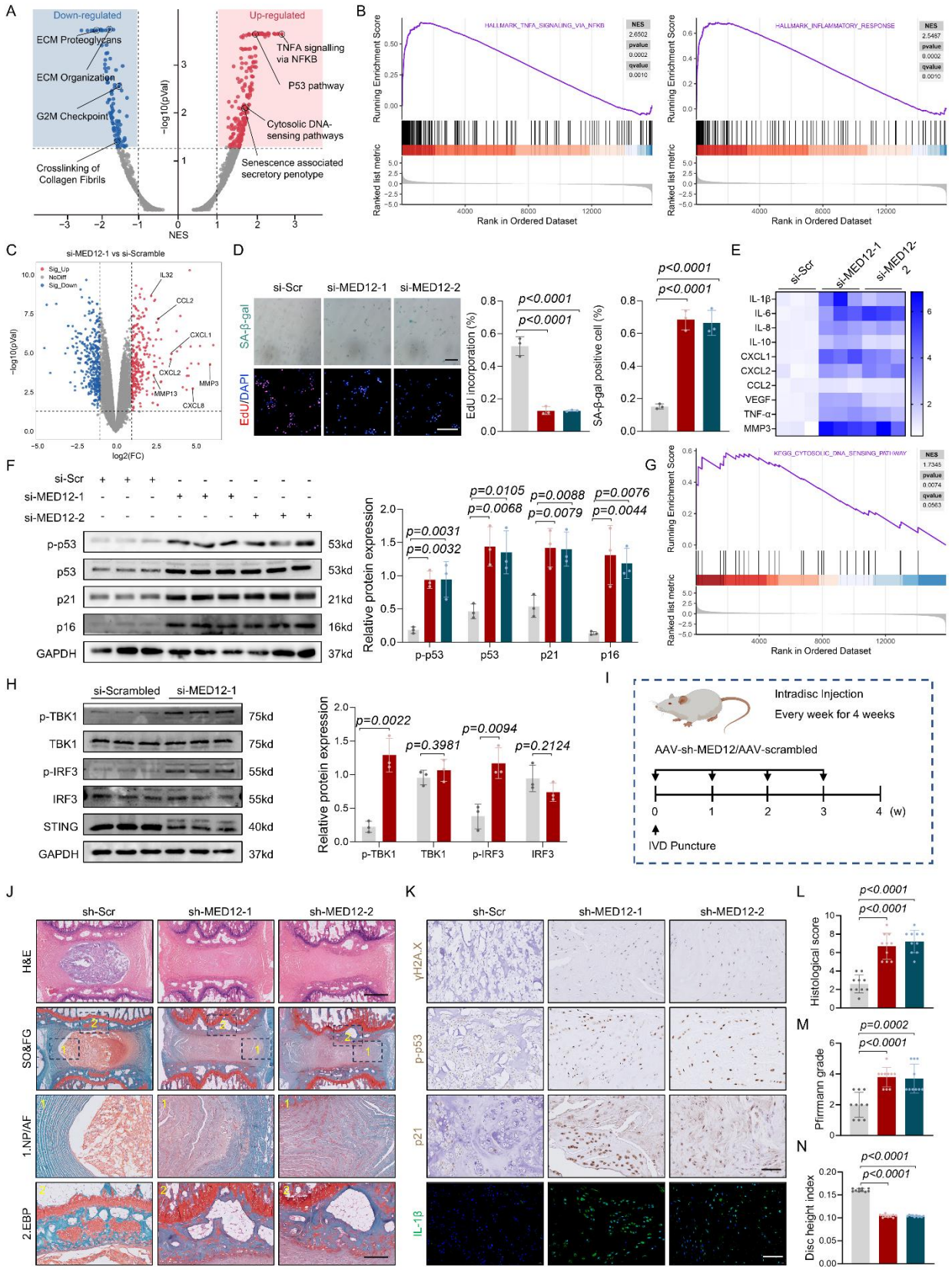
A
Down-regulated
Up-regulated
ECM Proteoglycans
ECM Organization
G2M Checkpoint
Crosslinking of Collagen Fibrils
TNFA signalling via NFKB
P53 pathway
Cytosolic DNA-sensing pathways
Senescence associated secretory penotype
−log10(pVal)
NES
B
HALLMARK_TNFA_SIGNALING_VIA_NFKB
HALLMARK_INFLAMMATORY_RESPONSE
Running Enrichment Score
Ranked list metric
Rank in Ordered Dataset
C
si-MED12-1 vs si-Scramble
Sig_Up
NoDiff
Sig_Down
IL32
CCL2
CXCL1
CXCL2
MMP3
MMP13
CXCL8
log2(FC)
D
si-Scr
si-MED12-1
si-MED12-2
SA-β-gal
EdU/DAPI
EdU incorporation (%)
SA-β-gal positive cell (%)
p<0.0001
E
IL-1β
IL-6
IL-8
IL-10
CXCL1
CXCL2
CCL2
VEGF
TNF-α
MMP3
F
si-Scr
si-MED12-1
si-MED12-2
p-p53
p53
p21
p16
GAPDH
53kd
21kd
16kd
37kd
Relative protein expression
p=0.0031
p=0.0032
p=0.0105
p=0.0068
p=0.0088
p=0.0079
p=0.0076
p=0.0044
G
KEGG_CYTOSOLIC_DNA_SENSING_PATHWAY
H
si-Scrambled
si-MED12-1
p-TBK1
TBK1
p-IRF3
IRF3
STING
GAPDH
75kd
55kd
40kd
37kd
p=0.0022
p=0.3981
p=0.0094
p=0.2124
I
Intradisc Injection
Every week for 4 weeks
AAV-sh-MED12/AAV-scrambled
0
1
2
3
4 (w)
IVD Puncture
J
sh-Scr
sh-MED12-1
sh-MED12-2
H&E
SO&FG
1.NP/AF
2.EBP
K
γH2A.X
p-p53
p21
IL-1β
L
Histological score
M
Pfirrmann grade
p=0.0002
N
Disc height index

855

Figure 6. MED12 deficiency promoted cGAS/STING axis-dependent senescence of NP cells during IVDD progression

(**A**) Volcano plot showing enriched down-regulated and up-regulated pathways of transcriptional profiles in NPCs transfected with si-MED12-1. (**B**) GSEA showing "Inflammatory response" and "TNFA signalling via NFKB" enriched in NP cells transfected with si-MED12-1. (**C**) Volcano plot analysis of the RNA-seq dataset illustrating the top upregulated and downregulated genes in MED12-silenced NPCs compare to control NPCs (**D**) SA-β-gal activity staining and EdU incorporation assay of NP cells transfected with si-MED12 (Scale bar: 100 μm). (**E**) Heatmap of differential SASP in NP cells transfected with si-MED12.IF staining of γH2A foci of NP cells transfected with si-MED12. (**F**). Protein level analysis of p-p53, p53, p21, p16 in NP cells transfected with si-MED12 by western blot. (**G**) GSEA showing "Cytosolic DNA-sensing pathway" enriched in NP cells transfected with si-MED12-1. (**H**) Protein level analysis of p-TBK1, TBK1, p-IRF3, IRF3, STING in NP cells transfected with si-MED12-1 by western blot. (**I**) Schematic illustration of the experiment design. (**J**). H&E staining SO&FG staining of coccygeal vertebrae from rats with the indicated treatment (Scale bar: 1 mm, 250 μm). (**K**). IHC staining and IF staining of p-p53, γH2A.X, p21 and IL-1β in rat coccygeal IVDs (Scale bar: 100 μm). (**L**) Histological score (n = 10), (**M**) Pfirrmann degenerative grades (n = 10), and (**N**) disc height index (n = 10) of rat coccygeal IVDs. Unpair students' t test (**H**) were used to performed, and data are represented as mean ± SD. One-way ANOVA (**D, F, L**, **M**, **N**) was used to performed, and data are represented as mean ± SD. At least 3 independent experiments were performed.

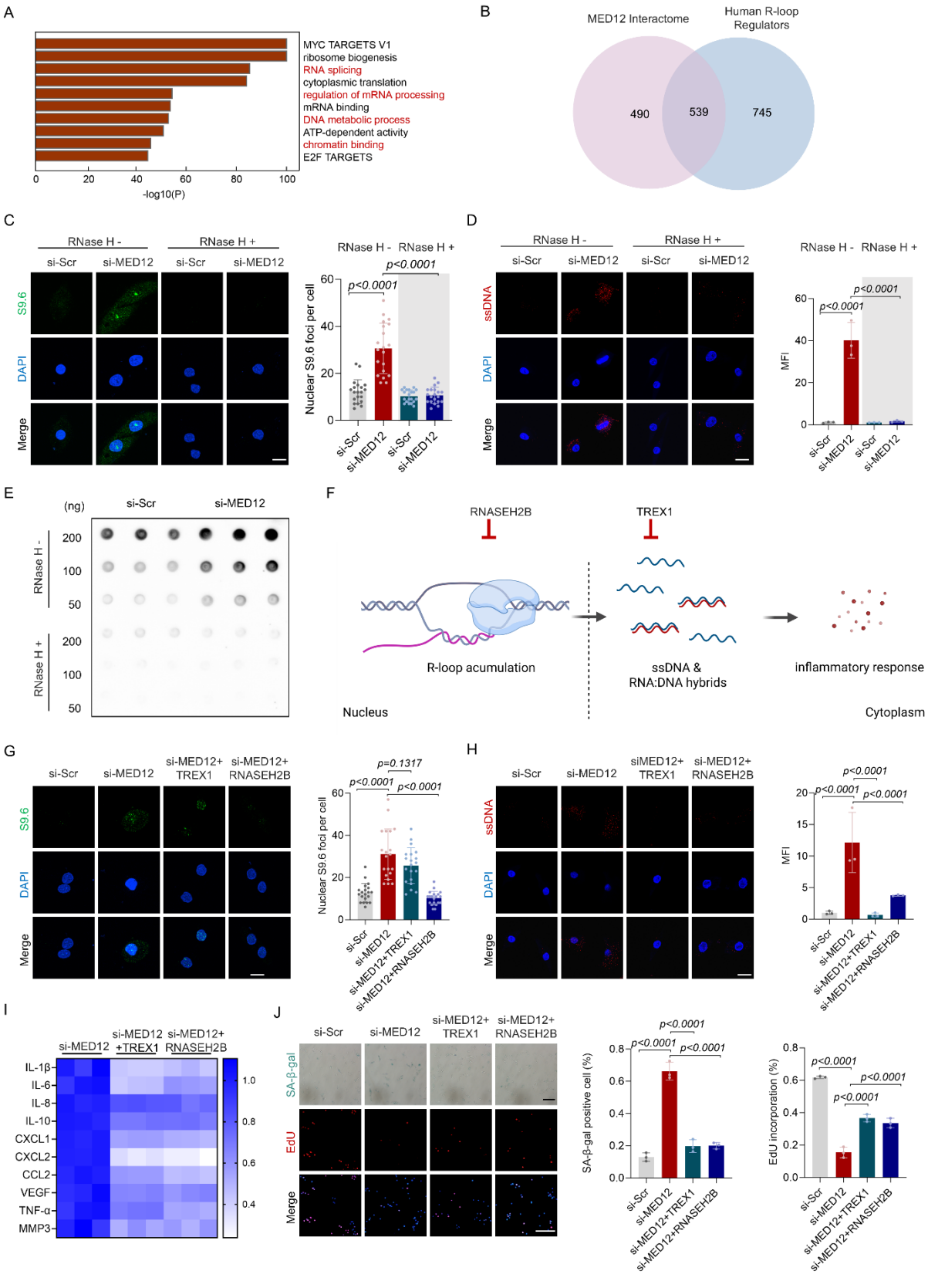
A
MYC TARGETS V1
ribosome biogenesis
RNA splicing
cytoplasmic translation
regulation of mRNA processing
mRNA binding
DNA metabolic process
ATP-dependent activity
chromatin binding
E2F TARGETS
-log10(P)
B
MED12 Interactome
Human R-loop Regulators
490
539
745
C
RNase H -
RNase H +
si-Scr
si-MED12
S9.6
DAPI
Merge
Nuclear S9.6 foci per cell
p<0.0001
D
ssDNA
MFI
E
(ng)
RNase H -
RNase H +
F
RNASEH2B
TREX1
R-loop acumulation
ssDNA &
RNA:DNA hybrids
inflammatory response
Nucleus
Cytoplasm
G
si-MED12+ TREX1
si-MED12+ RNASEH2B
p=0.1317
H
siMED12+ TREX1
I
IL-1β
IL-6
IL-8
IL-10
CXCL1
CXCL2
CCL2
VEGF
TNF-α
MMP3
J
SA-β-gal
EdU
SA-β-gal positive cell (%)
EdU incorporation (%)

879

Figure 7. MED12 loss induces R-loop accumulation, which drives NP cell senescence

(**A**) Enrichment analysis with Metascape showing terms for protein immunoprecipitated with MED12. (**B**) Venn diagram showing MED12 interactome overlapped with known R-loop regulators. (**C**) Representative IF image of MED12-depletion NP cells stained with S9.6 (green) and DAPI (blue) (Scale bar: 10 μm). (**D**) Representative IF image of MED12-depletion NP cells stained with ssDNA (red) and DAPI (blue) (Scale bar: 10 μm). (**E**) Dot blot analysis to quantify R-loops in NP cells transfected with si-MED12. RNaseH1 treatment was included as a negative control. (**F**) Schematic illustration of the functional role of abnormal accumulation of pathologic R-loops in chronic inflammation. (**G**) IF staining of R-loop in NP cells with the indicated treatment (Scale bar: 10 μm). (**H**) IF staining of ssDNA in NP cells with the indicated treatment (Scale bar: 10 μm). (**I**) Heatmap of differential SASP in NP cells with the indicated treatment. (**J**) SA-β-gal activity staining and EdU incorporation assay of NP cells transfected with si-MED12 (Scale bar: 100 μm). One-way ANOVA (**C, D, G**, **H**, **J**) was used to performed, and data are represented as mean ± SD. At least 3 independent experiments were performed.

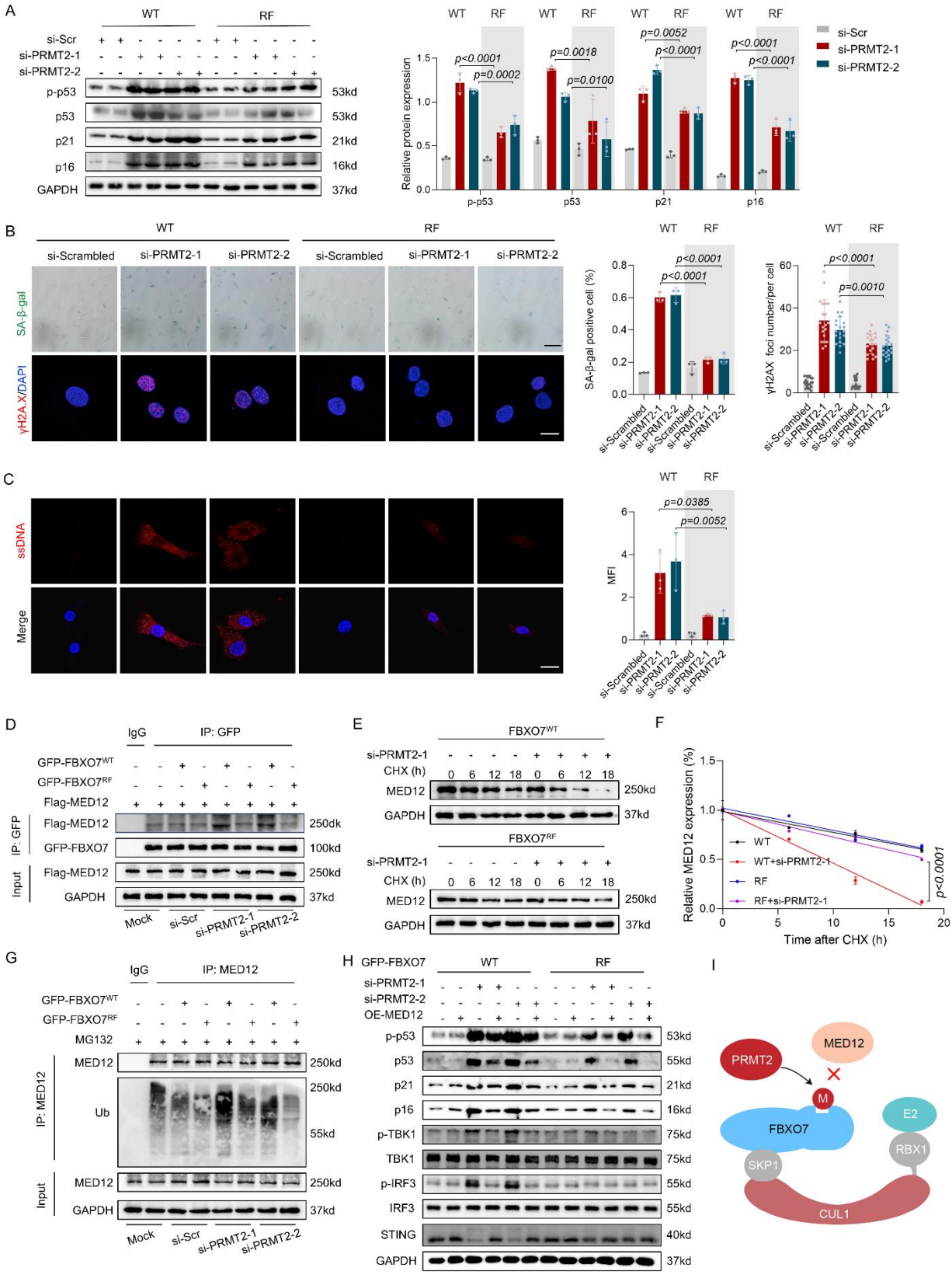
A
WT
RF
si-Scr
si-PRMT2-1
si-PRMT2-2
p-p53
p53
p21
p16
GAPDH
53kd
53kd
21kd
16kd
37kd
Relative protein expression
p<0.0001
p=0.0002
p=0.0018
p=0.0100
p=0.0052
p<0.0001
p<0.0001
p<0.0001
B
si-Scrambled
SA-β-gal
γH2A.X/DAPI
SA-β-gal positive cell (%)
γH2AX foci number/per cell
p<0.0001
p=0.0010
C
ssDNA
Merge
MFI
p=0.0385
p=0.0052
D
IgG
IP: GFP
GFP-FBXO7WT
GFP-FBXO7RF
Flag-MED12
IP: GFP
GFP-FBXO7
Input
250dk
100kd
250kd
37kd
Mock
si-Scr
si-PRMT2-1
si-PRMT2-2
E
FBXO7WT
FBXO7RF
si-PRMT2-1
CHX (h)
0 6 12 18 0 6 12 18
MED12
GAPDH
250kd
37kd
F
Relative MED12 expression (%)
Time after CHX (h)
WT
WT+si-PRMT2-1
RF
RF+si-PRMT2-1
p<0.0001
G
IP: MED12
MG132
Ub
55kd
H
GFP-FBXO7
OE-MED12
p-TBK1
TBK1
p-IRF3
IRF3
STING
40kd
I
PRMT2
MED12
M
FBXO7
E2
RBX1
SKP1
CUL1

894

Figure 8. Loss of PRMT2 promotes FBXO7-MED12-R-loop axis-dependent NPC senescence

(**A**) Protein level analysis of p-p53, p53, p21, p16 in NP cells with the indicated treatment by western blot. (**B**) SA-β-gal activity staining and IF staining of γH2A.X in NPCs with the indicated treatment (Scale bar: 100 μm, 10 μm). (**C**) IF staining of ssDNA in NP cells with the indicated treatment (Scale bar: 10 μm). (**D**) Co-IP analysis of the interaction of FBXO7 with MED12 in HEK293T cells cotransfected with Flag-MED12 and GFP-FBXO7 (wild-type and RF mutants) with or without si-PRMT2 transfection. (**E** and **F**) Half-life analysis of MED12 protein in NP cells cotransfected with Flag-MED12 and GFP-FBXO7 (wild-type, RF mutants) with or without si-PRMT2 transfection. (**G**) Co-IP analysis of endogenous MED12 ubiquitination in NPCs transfected with wild-type FBXO7 or FBXO7 RF mutant with or without si-PRMT2 transfection. (**H**) Protein level analysis of p-p53, p53, p21, p16, p-TBK1, TBK1, p-IRF3, IRF3, STING in NP cells with the indicated treatment by western blot. (**I**) A model of FBXO7-mediated MED12 protein polyubiquitination disrupted by the PRMT2. At least 3 independent experiments were performed.

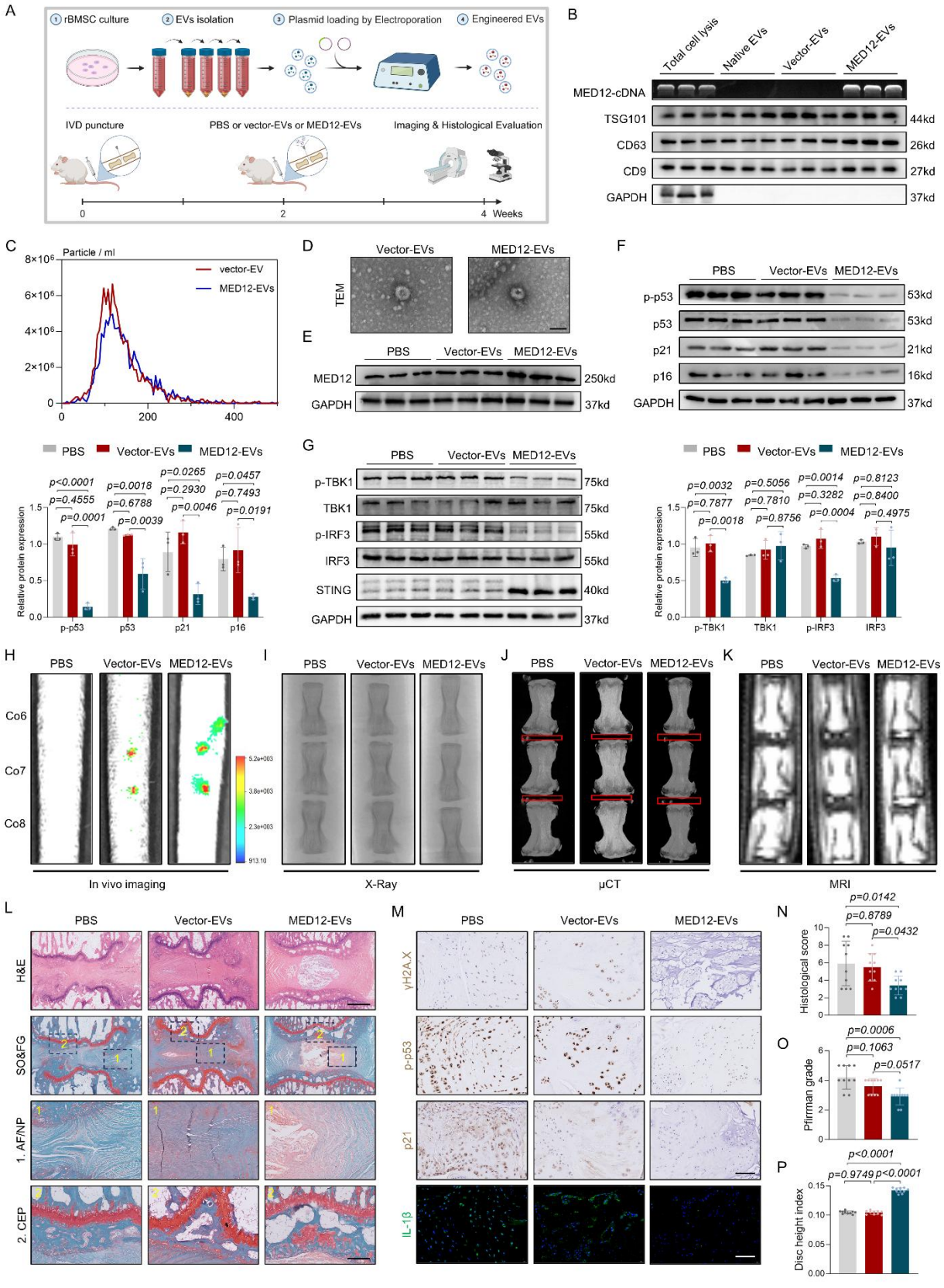
A
rBMSC culture
EVs isolation
Plasmid loading by Electroporation
Engineered EVs
IVD puncture
PBS or vector-EVs or MED12-EVs
Imaging & Histological Evaluation
0
2
4 Weeks
B
Total cell lysis
Native EVs
Vector-EVs
MED12-EVs
MED12-cDNA
TSG101
CD63
CD9
GAPDH
44kd
26kd
27kd
37kd
C
Particle / ml
vector-EV
MED12-EVs
D
TEM
Vector-EVs
MED12-EVs
E
PBS
Vector-EVs
MED12-EVs
MED12
GAPDH
250kd
37kd
F
PBS
Vector-EVs
MED12-EVs
p-p53
p53
p21
p16
GAPDH
53kd
53kd
21kd
16kd
37kd
Relative protein expression
p-p53
p53
p21
p16
G
p-TBK1
TBK1
p-IRF3
IRF3
STING
GAPDH
75kd
75kd
55kd
55kd
40kd
37kd
p-TBK1
TBK1
p-IRF3
IRF3
H
Co6
Co7
Co8
In vivo imaging
I
X-Ray
J
μCT
K
MRI
L
H&E
SO&FG
1. AF/NP
2. CEP
M
γH2A.X
p-p53
p21
IL-1β
N
Histological score
O
Pfirrman grade
P
Disc height index

910

Figure 9. EV-based MED12-overexpressing plasmid cargo alleviated NP cell senescence and IVDD progression

(**A**) Schematic illustration showing the experiment design. (**B**) Western blotting analysis of EV markers and cDNA electrophoresis to determine the efficiency of the MED12-overexpressing plasmid loading into rBMSC-derived EVs. (**C**) Nanoparticle tracking analysis (NTA) of ATR-EVs or vector-EVs. (**D**) Representative TEM images of EVs loading with MED12-overexpressing (MED12-EVs) or vector plasmid (vector-EVs) (Scale bar: 100 nm). (**E**) Protein level analysis of MED12 in rat NP cells with the indicated treatment by western blot. (**F**) Protein level analysis of p-p53, p53, p21, p16 in rat NP cells with the indicated treatment by western blot. (**G**) Protein level analysis of p-TBK1, TBK1, p-IRF3, IRF3, STING, in rat NP cells with the indicated treatment by western blot. Representative (**H**) In vivo imaging, (**I**) X-ray images, (**J**) μCT images, (**K**) MRI images of coccygeal vertebrae and IVDs from rats treated with the intradiscal injection of MED12-EVs or vector-EVs (**L**) H&E staining SO&FG staining of coccygeal vertebrae from rats with the indicated treatment (Scale bar: 1 mm, 250 μm). (**M**). IHC staining and IF staining of p-p53 and γH2A.X, p21 and IL-1β in rat coccygeal IVDs (Scale bar: 100 μm). (**N**) Histological score (n = 10) of rat coccygeal IVDs, (**O**) Pfirrmann degenerative grades (n = 10), and (**P**) Disc height index (n = 10). One-way ANOVA (**F, G, N**, **O**, **P**) was used to performed, and data are represented as mean ± SD. At least 3 independent experiments were performed.

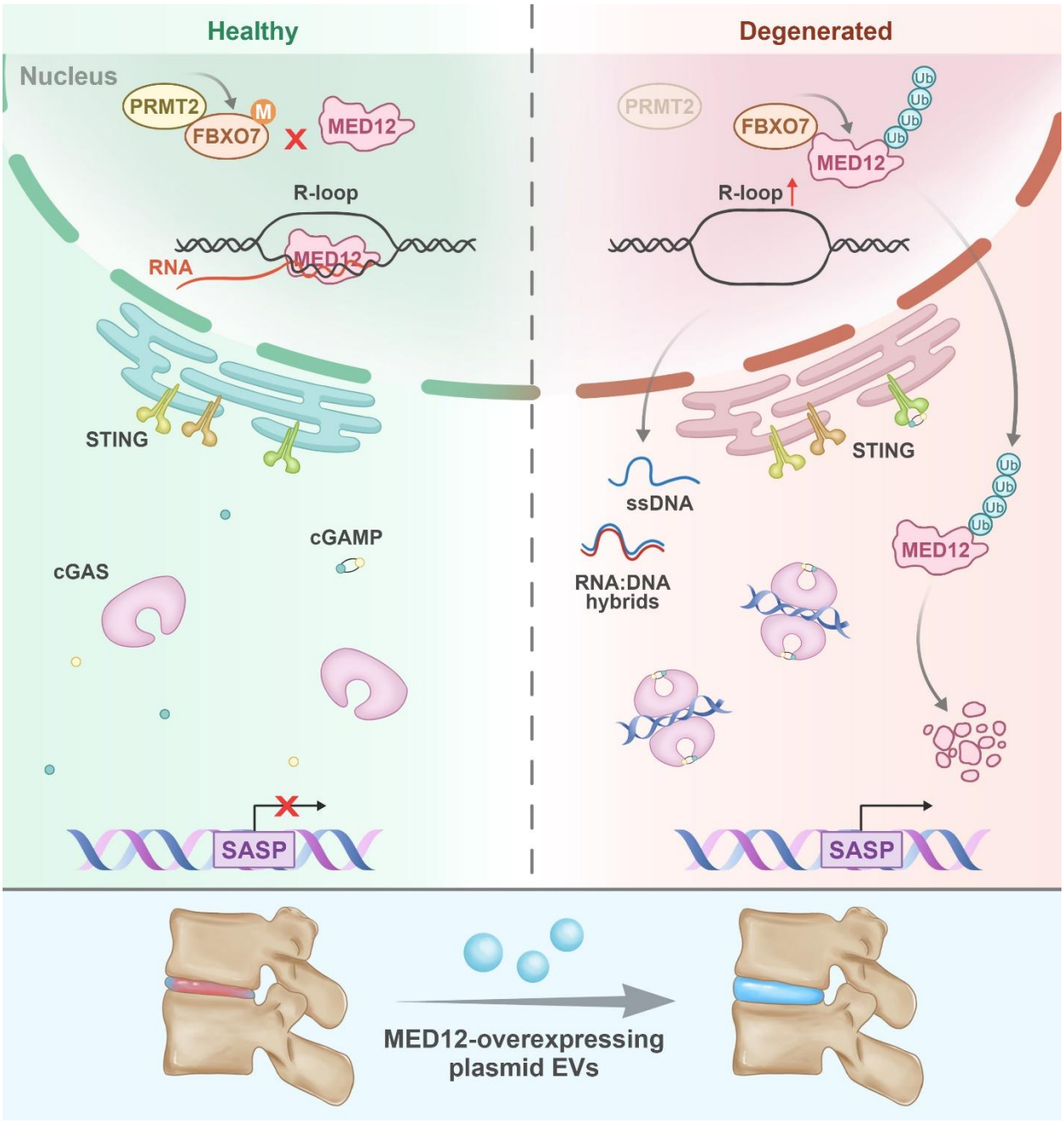

Figure 10. PRMT2 deficiency–mediated FBXO7-MED12 complex assembly promotes MED12 destabilization and R-loop/cGAS/STING axis-dependent intervertebral disc degeneration

Schematic illustration showing a mechanism linking methylation-ubiquitination crosstalk of MED12 and R-loop/cGAS/STING axis in NP cell senescence and IVDD progression.